UNIVERSITY OF PADOVA

DEPARTMENT OF MANAGEMENT AND ENGINEERING DTG

MASTER'S THESIS IN MANAGEMENT ENGINEERING

Interlocking effect on residual stress and distortion of Laser-Welded A304 steel plates

SUPERVISOR

PROF.PAOLO FERRO

MASTERCANDIDATE

MOHAMMAD JAVANMARDI JALALABADI

STUDENT ID

2043106

Academic Year

2023-2024

Master Thesis

Master of science in Management Engineering

Interlocking effect on residual stress and distortion of Laser-Welded A304 steel plates

Author:

Mohammad Javanmardi Jalalabadi

Supervisor:

Paolo Ferro

To my family

تقدیم به خانواده ام

To my friends

تقدیم به دوستانم

Abstract (EN)

Laser welding is widely used in industries for the assembly of various products such as ships, automobiles, trains, and bridges. Residual stress and welding distortion often result in dimensional inaccuracies during assembly and increased construction costs. Therefore, predicting and reducing welding distortion is crucial for improving the quality of welded structures. This research focuses on the analysis of residual stress and distortion in two laser-welded A304 steel pieces. Standard and interlocking welding methods were employed for the joints. Optical microscopy was used to examine the microstructure. Mechanical behavior was assessed through tensile testing, microhardness measurement, residual stress, and distortion analysis. Residual stress in different welding zones was measured using X-ray diffraction. The results indicated that the metal's microstructure in the weld is austenitic with skeletal ferrite in some areas. The microhardness of the standard weld metal increases by approximately 22% compared to the base metal, attributed to the formation of a skeletal ferrite phase in the weld metal while this value is 11% for the Interlocking one. The yield and tensile strength of the interlocking-welded sample increased by about 8% and 1.2%, respectively, compared to the standard-welded sample. Distortion results showed a 12.6% and 10.5% change in the angle for standard welding and Interlocking welding compared to the baseline. Additionally, changes in height for Standard and Interlocking welding were approximately 5.2% and 28.9%, respectively, compared to the baseline.

Keywords: Laser welding, A304 stainless steel, residual stress, distortion, microstructure

Abstract (IT)

La saldatura laser è ampiamente utilizzata nelle industrie per l'assemblaggio di vari prodotti come navi, automobili, treni e ponti. Lo stress residuo e la distorsione durante la saldatura spesso causano inaccuratezze dimensionali durante l'assemblaggio e un aumento dei costi di costruzione. Pertanto, prevedere e ridurre la distorsione durante la saldatura è cruciale per migliorare la qualità delle strutture saldate. Questa ricerca si concentra sull'analisi dello stress residuo e della distorsione in due pezzi di acciaio A304 saldati al laser. Sono stati impiegati metodi di saldatura standard e a incastro per le giunzioni. La microscopia optical è stata utilizzata per esaminare la microstruttura. Il comportamento meccanico è stato valutato attraverso prove di trazione, misurazione della microdurezza, analisi dello stress residuo e della distorsione. Lo stress residuo nelle diverse zone di saldatura è stato misurato utilizzando la diffrazione dei raggi X. I risultati indicano che la microstruttura del metallo nella saldatura è austenitica con ferrite scheletrica in alcune aree. La microdurezza del metallo saldato in modo standard aumenta di circa il 22% rispetto al metallo di base, attribuito alla formazione di una fase di ferrite scheletrica nel metallo saldato, mentre questo valore è del 11% per quello a incastro. La resistenza alla trazione e la resistenza ultima del campione saldato a incastro aumentano rispettivamente del 8% e dell'1,2% rispetto al campione saldato in modo standard. I risultati della distorsione mostrano una variazione dell'angolo del 12,6% e del 10,5% per la saldatura standard e quella a incastro rispetto alla linea di base. Inoltre, le variazioni in altezza per la saldatura standard e quella a incastro sono approssimativamente del 5,2% e del 28,9%, rispettivamente, rispetto alla linea di base.

Parole chiave: Saldatura laser, acciaio inossidabile A304, stress residuo, distorsione, microstruttura

Content page

Tables

Title **page**

Figures

Title **page**

Chapter 1: Introduction

One of the most important goals of industrial designers is the optimal use of components and understanding their capabilities, reliability, and efficiency. This enables them to make the best use of the existing components. Many factors significantly impact the quality of welded parts. Undoubtedly, one of the most crucial factors is the presence of residual stress and distortion in the components.

Residual stresses are stresses that exist in the absence of external loads. All processes that result in plastic deformation lead to the creation of some type of residual stresses in the component. Identifying these types of stresses is crucial for the proper and optimal use of components. The presence of residual stresses in components can, in some cases, enhance performance, while in others, it may lead to a decrease in performance. In sensitive applications where the component must have exceptional performance, the identification of such stresses becomes essential. For example, the issue of residual stresses in sensitive applications such as aerospace, maritime, ship hulls, pressure vessels, oil and gas transmission lines, and nuclear reactors doubles in importance for ensuring the health of components and extending their service life.

The joining of metals using lasers became inevitable in engineering industries for both technical and economic reasons. The welding of metals using lasers was widely used in the fabrication of microsystems such as Micro Electro Mechanical Systems, Automotive - inner and outer car door panels, fuel tanks, and roof and pillar channels, Marine industries -for welding of deck plate, baffle plates, boilers and household utensils and others. The adoption of a metal helps to obtain the flexibility and complex design of products for getting specific properties as per functional requirements. In the laser welding process, the material undergoes rapid heating and cooling. During this process, non-uniform expansion and contraction of the weld pool region and base metals occur, resulting in distortion and development of residual stresses which remain in the weld joints without any external loading. The residual stresses are classified as macro stresses and micro stresses. The macro stresses are self-equilibrated, long-range stresses produced in regions around the weld, whereas, micro stresses are homogenous or inhomogeneous and short-range stresses.

Various methods exist for generating residual stresses, providing different types and levels of residual stresses. Among these methods, we can mention: non-uniform deformation due to external factors (such as hammering, forging, machining, turning, etc.), plastic deformation resulting from uneven thermal changes (quenching, LSP, etc.), phase transformations, structural and chemical heterogeneity in the material (nitriding, localized heating, etc.), surface operations (coating, shaping, PVD, CVD, etc.), and differences in the thermal expansion coefficients of the elements.

Welding processes are widely used in many industries for producing lighter and simpler components. In this process, regions farther from the weld metal prevent the expansion and contraction of the weld metal and the base metal nearby. Therefore, after cooling to ambient temperature, residual tensile stresses remain in the weld metal, and residual compressive stresses exist in regions farther from it.

The results of numerous studies and research in this field have shown that tensile residual stresses generally have negative effects on the fracture of specimens, while compressive residual stresses have positive effects on the fatigue life of specimens, increasing their endurance. Therefore, depending on the application and sensitivity of the components, there is a need for a careful examination of the type and distribution of stresses. There are various methods for measuring these residual stresses, but only a few of them have the capability to measure stresses at different locations on a specimen.

Different methods exist for measuring or estimating residual stresses based on precise measurements or using numerical techniques. Measurements can be destructive, such as drilling, semi-destructive, or non-destructive, such as X-rays, neutron diffraction, and ultrasonic methods. Precise methods used for evaluating residual stresses are often of a destructive nature.

Today, the effort to measure and reduce residual stress and distortion in welding continues. Considering that there have been no studies on welding, investigating residual stress and distortion in laser-welded A304 steel components in scientific literature, it is essential to conduct sufficient research in this regard to obtain desired results. Given the impact of welding residual stress on the properties of the resulting weld, this study focuses on examining and measuring the residual stress and distortion resulting from the connection of two A304 stainless steel sheets using the laser welding method, employing X-ray techniques.

Continuing, in the second chapter, an introduction is provided to the raw materials, methods of their connection, residual stress, sources of residual stress generation, and methods of measurement, along with a review of relevant studies. The third chapter covers the materials used, the work procedure, conducted tests, standards, and the equipment utilized. Finally, the test results are presented, discussed in the context of the examined evidence, and recommendations for future work are provided.

Chapter 2 – State of Art

2-1 Stainless Steels

Stainless steels are a group of high-alloy steels based on the Fe-Cr, Fe-Cr-C, and Fe-Cr-Ni systems. These Steels must contain a minimum of 10.5% chromium by weight in order to be considered stainless [1]. This level of chromium content creates a passive oxide surface that prevents oxidation and corrosion of the underlying metal in non-corrosive environments. Stainless steels exhibit excellent resistance to oxidation, even at high temperatures, and are often categorized as heat-resistant alloys. The resistance to oxidation at elevated temperatures is primarily a function of the chromium content, and some alloys containing around 25% to 30% by weight of chromium can be used at high temperatures, such as 1000 degrees Celsius [2 and 3]. Stainless steels are also classified based on their metallurgical structure and chemical composition, as follows:

- Ferritic Stainless Steel
- Martensitic Stainless Steel
- Austenitic Stainless Steel
- Duplex Stainless Steel (Austenitic-Ferritic)
- Precipitation-Hardening Stainless Steel

2-1-1 Austenitic Stainless Steels

Austenitic stainless steels are the largest and most common group of stainless steels, produced in higher quantities compared to other groups. They are essentially ternary alloys of Fe-Cr-Ni with 16-20% chromium and 7-20% nickel. Since the structure of these steels remains austenitic (γ-iron) at all practical temperatures during heat treatment, they are referred to as austenitic stainless steels. In these stainless steels, the presence of nickel in the range of 6 to 22% is essential to stabilize the austenitic structure. Their strength is comparable to that of mild steels. The minimum yield strength of these steels at room temperature is 210 megapascals (MPa). This type of steel typically exhibits good

ductility and toughness and, under tensile loading, can show a significant increase in length without fracturing [4].

Austenitic stainless steels do not have the capability for phase transformation hardening, meaning they cannot be hardened through heat treatment processes. Due to the presence of retained austenite at room temperature, this type of austenitic steel is highly ductile and typically exhibits better corrosion resistance compared to ferritic types. Many austenitic stainless steels require special heat treatment and modified chemical compositions to prevent intergranular corrosion. Most of these steels are based on the 18Cr-10Ni system with additional alloying elements and modifiers to create specific properties or improve performance. Type 304 is the fundamental alloy in this group, and among austenitic types, 304L is the most common choice [4].

2-1-2 Alloys and Standard Consumables

Austenitic stainless steels, according to the American Iron and Steel Institute (AISI) standard, are divided into series 200 and 300. Series 200 alloys contain higher amounts of carbon, manganese, and nitrogen and are used in special applications where wear and abrasion resistance are required. Furthermore, the nickel content in these alloys is lower compared to the alloys in series 300 to balance the higher levels of carbon and nitrogen. Alloys in the 300 series are the most used among austenitic stainless steels. A list of commonly used alloys in the 300 series is provided in Table 1. The most used alloys in this group include types 304, 316, 321, and 347, along with their derivatives. Some of the filler metals for austenitic stainless steels are shown in Table 2. These consumables can be used in the form of shielded metal arc electrodes, solid wires, flux-cored wires, and submerged arc electrodes [5].

Table 1: shows the chemical composition of some commonly used alloys in the 300 series of austenitic stainless steels [5].

Alloy	Designation	C	N	Cr	Ni	Mo	Mn	Si	Other	Other	Other
201	S20100	0.08	0.07	16.3	4.5	0.2	7.1	0.45	0.001 S	0.03 P	0.2 Cu
201 drawing	S220100	0.08	0.07	16.9	5.4	0.02	7.1	0.5	0.001 S	0.30 P	0.6 Cu
201LN	S20153	0.02	0.13	16.3	4.5	0.2	7.1	0.45	0.001 S	0.03 P	0.5 Cu
301 tensile	S30100	0.08	0.4	16.6	6.8	0.2	1.0	0.45	0.001 S	0.03 P	0.3 Cu
301 drawing	S30100	0.08	0.04	17.4	7.4	0.02	1.7	0.45	0.007 S	0.03 P	0.6 Cu
303	S30300	...	...	...	...	...	...	...	...	...	...
304	S30400	0.05	0.05	18.3	8.1	0.3	1.8	0.45	0.001 S	0.03 P	0.3 Cu
304 drawing	S30400	0.05	0.04	18.4	8.6	0.3	1.8	0.45	0.001 S	0.03 P	0.3 Cu
304 extra drawing	S30400	0.06	0.04	18.3	9.1	0.3	1.8	0.45	0.001 S	0.030 P	0.4 Cu
304L tubing	S30403	0.02	0.09	18.3	8.1	0.3	1.8	0.45	0.013 S	0.030 P	0.4 Ci
305	S30500	0.05	0.02	18.8	12.1	0.2	0.8	0.60	0.001 S	0.02 P	0.2 Cu
321	S32100	0.05	0.01	17.7	9.1	0.03	1.0	0.45	0.001 S	0.03 P	0.4 Ti
316L	S31603	0.02	0.0	16.4	10.5	2.1	1.8	0.50	0.010 S	0.03 P	0.4 Cu

Table 2: displays the chemical composition of some well-known filler metals for austenitic stainless steels [5].

AWS Classification[d]	UNS Number[e]	Composition, Wt-%[b,c]										Other Elements	
		C	Cr	Ni	Mo	Mn	Si[a]	P	S	N	Cu	Element	Amount
ER209	S20980	0.05	20.5–24.0	9.5–12.0	1.5–3.0	4.0–7.0	0.90	0.03	0.03	0.10–0.30	0.75	V	0.10–0.30
ER218	S21880	0.10	16.0–18.0	8.0–9.0	0.75	7.0–9.0	3.5–4.5	0.03	0.03	0.08–0.18	0.75	—	—
ER219	S21980	0.05	19.0–21.5	5.5–7.0	0.75	8.0–10.0	1.00	0.03	0.03	0.10–0.30	0.75	—	—
ER240	S24080	0.05	17.0–19.0	4.0–6.0	0.75	10.5–13.5	1.00	0.03	0.03	0.10–0.30	0.75	—	—
ER307	S30780	0.04–0.14	19.5–22.0	8.0–10.7	0.5–1.5	3.30–4.75	0.30–0.65	0.03	0.03	—	0.75	—	—
ER308	S30880	0.08	19.5–22.0	9.0–11.0	0.75	1.0–2.5	0.30–0.65	0.03	0.03	—	0.75	—	—
ER308Si	S30881	0.08	19.5–22.0	9.0–11.0	0.75	1.0–2.5	0.65–1.00	0.03	0.03	—	0.75	—	—
ER308H	S30880	0.04–0.08	19.5–22.0	9.0–11.0	0.50	1.0–2.5	0.30–0.65	0.03	0.03	—	0.75	—	—
ER308L	S30883	0.03	19.5–22.0	9.0–11.0	0.75	1.0–2.5	0.30–0.65	0.03	0.03	—	0.75	—	—
ER308LSi	S30888	0.03	19.5–22.0	9.0–11.0	0.75	1.0–2.5	0.65–1.00	0.03	0.03	—	0.75	—	—
ER308Mo	S30882	0.08	18.0–21.0	9.0–12.0	2.0–3.0	1.0–2.5	0.30–0.65	0.03	0.03	—	0.75	—	—
ER308LMo	S30886	0.04	18.0–21.0	9.0–12.0	2.0–3.0	1.0–2.5	0.30–0.65	0.03	0.03	—	0.75	—	—
ER309	S30980	0.12	23.0–25.0	12.0–14.0	0.75	1.0–2.5	0.30–0.65	0.03	0.03	—	0.75	—	—
ER309Si	S30981	0.12	23.0–25.0	12.0–14.0	0.75	1.0–2.5	0.65–1.00	0.03	0.03	—	0.75	—	—
ER309L	S30983	0.03	23.0–25.0	12.0–14.0	0.75	1.0–2.5	0.30–0.65	0.03	0.03	—	0.75	—	—

2-1-3 Welding of Austenitic Stainless Steels

Austenitic stainless steels have very high weldability and can be welded using all fusion and resistance welding processes. Due to their good weldability, wide range of applications, and versatility, austenitic stainless steels are used in the construction of pressure vessels, storage tanks, chemical plants, and household applications. Welds in austenitic stainless steels typically have chemical composition, mechanical properties, and ductility that can be compared to the base metals [6]. Two important points to consider when creating welds in austenitic stainless steels are:

• Protection against corrosion

• Avoiding corrosion cracking

2-1-4 Solidification of Austenitic Stainless Steels

In general, in weld metals derived from austenitic filler metals, four types of solidification and phase transformation in the solid state are possible, as shown in Table 3. The relationship between the type of solidification and the pseudo-binary phase diagram in Figure 1 is provided. Solidification modes A and AF correspond to solidifications that occur with primary austenite, where austenite is the first phase formed during solidification. Types of solidification FA and F have primary delta ferrite phase. Subsequently, after solidification FA and F, due to the instability of delta ferrite at lower temperatures, other microstructural changes also occur [7].

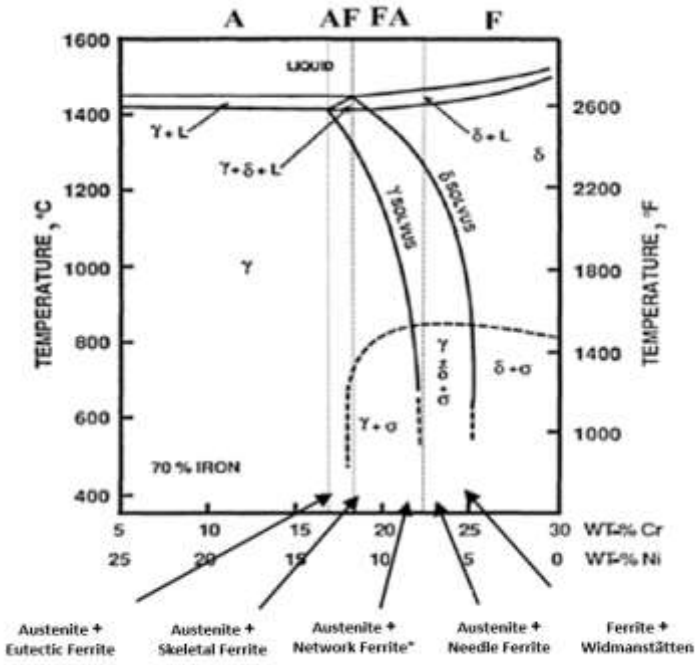

Figure 1: Relationship between the type of solidification and the pseudo-binary phase diagram [7].

Table 3: Types of Solidification, Reactions, and Microstructures Resulting from Stainless Steel [7]

microstructure	reaction	Type of solidification.
Fully austenitic, completely defined solidification structure.	L→ L+A→ A	A
"Ferrite at the boundaries of cells and dendrites."	L→ L+A→ L+A+(A+F) →A+F	AF
"Ferrite skeletal or network resulting from ferrite transformation to austenite."	L→ L+F→ L+F+(F+A)→ F+A	FA
"Needle-like ferrite with ferritic background, austenitic boundary and Widmanstätten side plates."	L→ L+F →F→ F+A	F

In a study conducted by David on various ferrite morphologies in multi-pass welds of austenitic stainless steels and weld metal 308, it was observed that the structure in the weld metal changes with an increase in the ferrite number, as shown in Figure 2. They found, by examining the effect of passes, that the ferrite percentage decreases in the upper passes in multi-pass welds, as illustrated in Figure 3 [8]. Smith and his colleagues also investigated the microstructure in series 300 stainless steels and

observed that the structure in the weld metal is variable with an increase in the chromium-to-nickel ratio, as shown in Figure 4. Figure 5 represents a schematic of the thermal and precipitation processes that occur in 316 stainless steel [9].

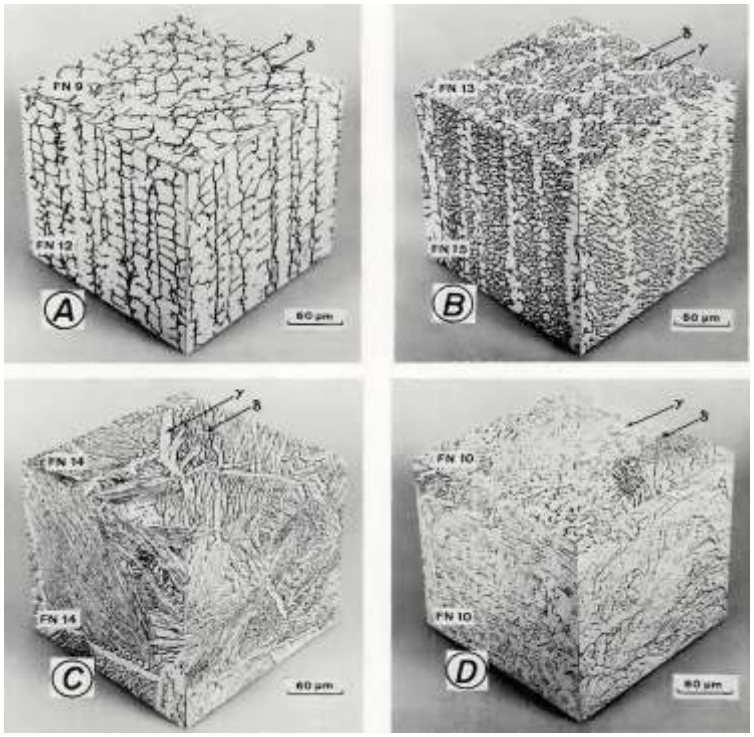

Figure 2: shows a three-dimensional representation of various ferrite morphologies in multi-pass welds of austenitic stainless steel 308." Wormlike, (B) Network, (C) Needle-like, and (D) Spherical [8].

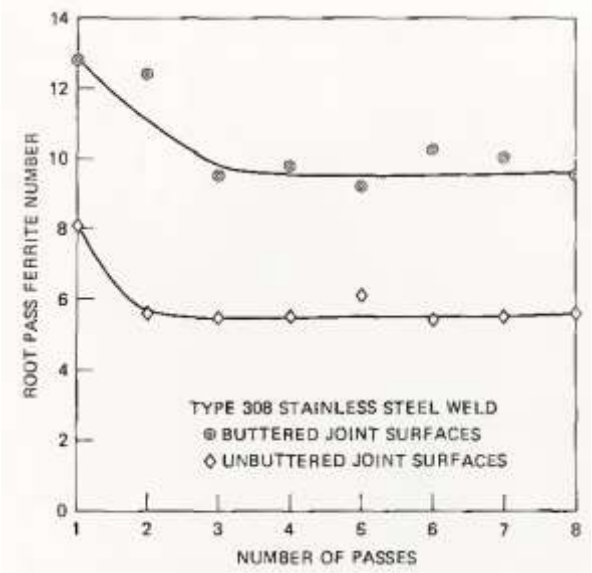

Figure 3: shows the changes in the ferrite percentage in the root pass compared to subsequent passes in the weld [8].

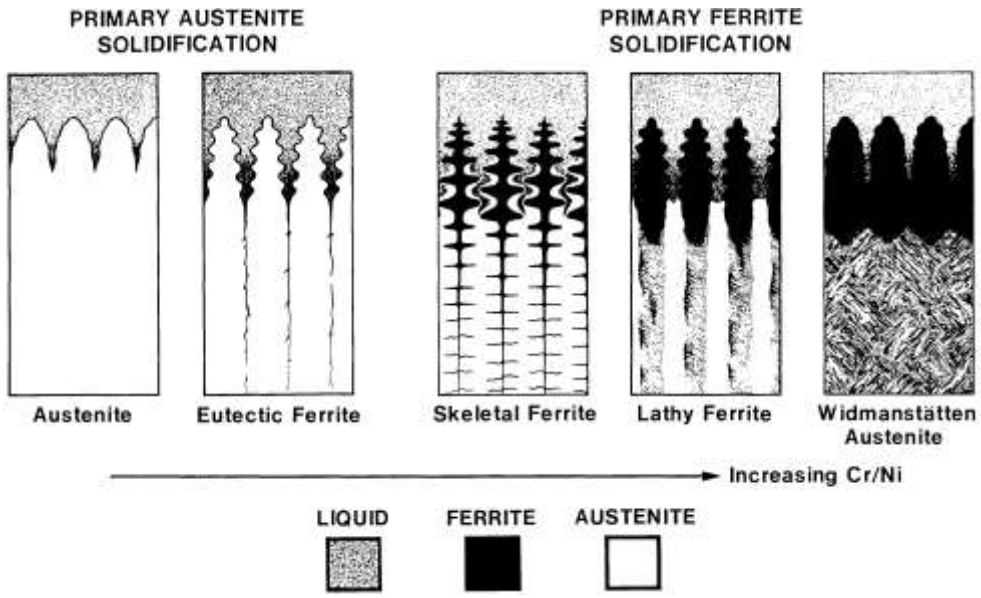

Figure 4: depicts a schematic summary of the solidification and transformation behavior of fully austenitic and two-phase microstructures [9].

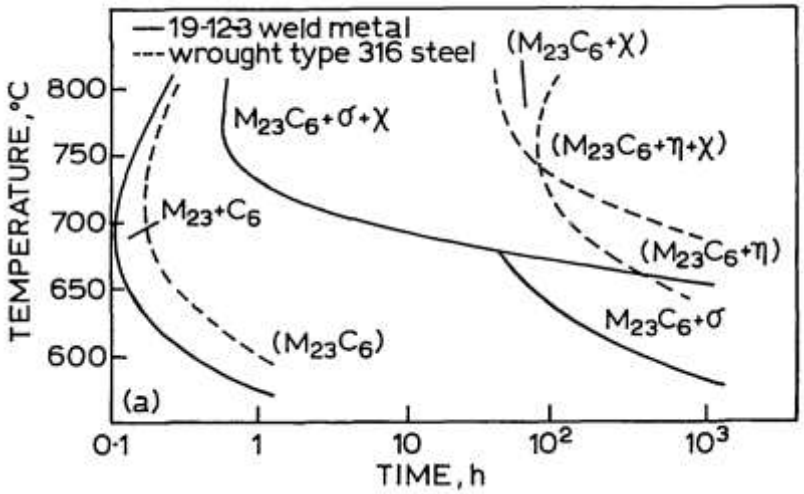

Figure 5: represents the temperature-time-precipitation diagram for the weld metal containing 19Cr-12Ni-3Mo [9].

2-2 Laser Welding Process

"Until the early 1970s, lasers were used as a source for welding thin metal sheets at low speeds. However, laser welding has been employed since 1965 in welding electronic circuit boards and in micro-welding, performed within a vacuum chamber. This was at a time when conventional welding methods were incapable of welding these materials. With the advancement of knowledge and the

emergence of continuous wave (CW) CO_2 and ND: YAG lasers, lasers have been used for deep welding applications in the past 20 years [10]. The laser's ability to deliver power per unit area ($\frac{w}{cm^2}$) is a critical factor in determining welding potential. Multiple experiments demonstrate that lasers create precise welds that are only comparable to welds created by electron beam welding (EBW) [10].

"Unlike electron beam welding (EBW), which requires a vacuum environment, laser beam welding (LBW) can be performed under shielding gases such as argon, helium, and CO_2. The laser welding process is controlled by modifying energy beam parameters. Unlike electron beam and manual electrode arc welding, lasers are not influenced by the magnetic field of the workpiece. As a result, it is possible to achieve desirable quality during welding. Both solid-state and gas-state laser welding methods can be used continuously and in pulsed mode as welding sources. Due to the high power per unit area of lasers during welding, the volume of molten metal is small, and the heat-affected zone (HAZ) is minimized. Moreover, the heat input (HI) is low, resulting in minimal distortion in the weld zone. With LBW, components with various dimensions, ranging from a few micrometers to several millimeters, can be welded [10].

Kumar et al. [11] were studied on Comparative study of pulsed Nd: YAG laser welding of AISI 304 and AISI 316 stainless steels. Laser welding is a potentially useful technique for joining two pieces of similar or dissimilar materials with high precision. They, were studied on laser welding of similar metal of AISI 304SS and AISI 316SS have been conducted forming butt joints. A robotic control 600 W pulsed Nd:YAG laser source has been used for welding purpose. The effects of laser power, scanning speed and pulse width on the ultimate tensile strength and weld width have been investigated using the empirical models developed by RSM. The results of ANOVA indicate that the developed models predict the responses adequately within the limits of input parameters. 3-D response surface and contour plots have been developed to find out the combined effects of input parameters on responses. Furthermore, microstructural analysis as well as hardness and tensile behavior of the selected weld of 304SS and 316SS have been carried out to understand the metallurgical and mechanical behavior of the weld. The selection criteria are based on the maximum and minimum strength achieved by the respective weld [11].

It has been observed that the current pulsation, base metal composition and variation in heat input have significant influence on controlling the microstructural constituents (i.e. phase fraction, grain size etc.). The result suggests that the low energy input pulsation generally produce fine grain structure and improved mechanical properties than the high energy input pulsation irrespective of base material composition. However, among the base materials, 304SS depict better microstructural and mechanical properties than the 316SS for a given parametric condition. Finally, desirability function analysis has

been applied for multi-objective optimization for maximization of ultimate tensile strength and minimization of weld width simultaneously. Confirmatory tests have been conducted at optimum parametric conditions to validate the optimization techniques [11].

Weld samples R9 and S5 have natural notch (reduced fusion zone area) at the fusion zone as shown in Figure 6 where local stress concentration is significantly high enough and may be the reason of sudden failure unlike other weld samples. It is likely to be mentioned here that the notch at sample R9 and sample S5 has been created due to the higher energy input and, is associated with them resulting in excessive melt along with large weld pool during welding which is unable to fill the weld crater during solidification [11].

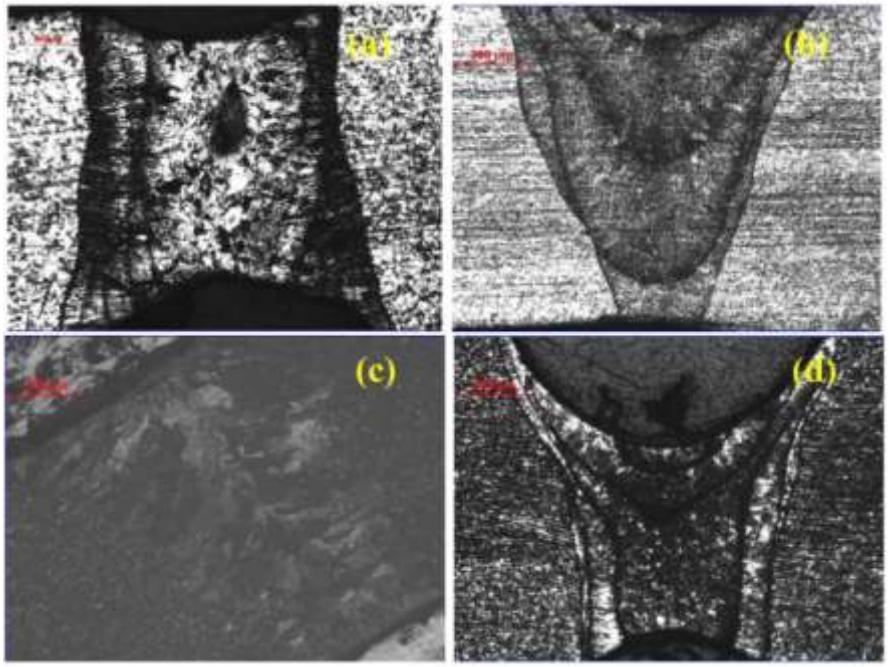

Figure 6: Macrographs show the fusion zone profiles of samples (a) R9, (b) R10, (c) S4 and (d) S5 [11].

Laser welding is a non-contact process that only requires access to one side of the workpiece. In this process, a molten and mixed zone of materials is created by the heat generated from the impact of a laser beam on the surface. After solidification, a connection between the materials is established. The laser beam is highly collimated and focused towards the workpiece's surface. When the laser beam is concentrated on the desired point, it rapidly melts the metal, creating a small and narrow weld zone with very high bonding efficiency while causing minimal damage to the workpiece. Precise control of the beam is necessary to ensure localized melting without spreading to the surroundings. The

characteristic of laser welding is the creation of a small molten zone by the energy absorbed at the narrow laser beam's impact point, essentially striking a balance between heating and cooling of a specific volume of one or two solid materials, resulting in the formation and solidification of molten material. This molten zone spreads at the common junction of the two solids, thereby creating a continuous connection between the two solid pieces [12].

2-2-1 Advantages, Limitations, and Applications of Laser Welding

The main advantages of laser welding that have increasingly caught the attention of engineers include [12]:

1. Precise control of heat input compared to other welding processes like GTAW and PAW.
2. High power density and short solidification time, enabling welding of metals and alloys with varying metallurgical compatibility and distinct physical and mechanical properties. Components may vary significantly in mass, dimensions, and electrical resistance.
3. No need for a vacuum (since laser beams can pass through air without significant energy loss).
4. Due to the high beam focus ability, it is possible to create small spot welds with diameters as small as a few thousandths of an inch.
5. Very high welding speeds, often reaching several meters per minute.
6. No heat-affected zone (HAZ) or an extremely narrow one if present.
7. Reduces residual stresses and minimizes discontinuities.
8. Due to its numerous advantages, laser welding is particularly suitable for applications where final dimensional accuracy is critical or for cases where high-volume production of welded parts is required.

In the laser welding process, like other welding processes, there are limitations and challenges, some of which include [12]:

1. If parts are not precisely aligned, edge cracking can occur unless filler metal is used.
2. The equipment and components of this system, such as the optical system, coolers, and other parts, are relatively expensive and must be manufactured with very high precision."
3. Materials with high optical reflectivity or high thermal conductivity can pose challenges in achieving effective melting.

4. Welding defects such as porosity can easily form in deep weld regions."

Laser welding, due to its unique characteristics, has found applications in various industries, including electrical and electronics, aerospace, military, giant generators, and the automotive industry [13]

2-2-2 Types of Laser Welding Modes

Laser welding can be performed in two modes:

- Conduction Mode
- Keyhole Mode

"The welding mode strongly influences the final weld dimensions. When a high-power laser beam strikes the material's surface, it absorbs a specific portion of the laser energy, along with heat conduction into the metal, leading to the formation of a molten pool. Heat conduction appears to be the primary mechanism of energy transfer, limiting the depth of penetration and the interaction time between the laser and the material. These welds are referred to as conduction mode welds. Since energy transfer to the metal and the formation of the molten pool are controlled by the heat conduction rate, despite some molten metal displacement, the shape of the weld pool is somewhat influenced. Conduction mode welds generally have a depth-to-width ratio of less than 0.5. The application of conduction mode welds is limited to thin samples due to their shallow penetration depth. Figure 9 schematically illustrates the conduction mode and keyhole (deep penetration) welds [14].

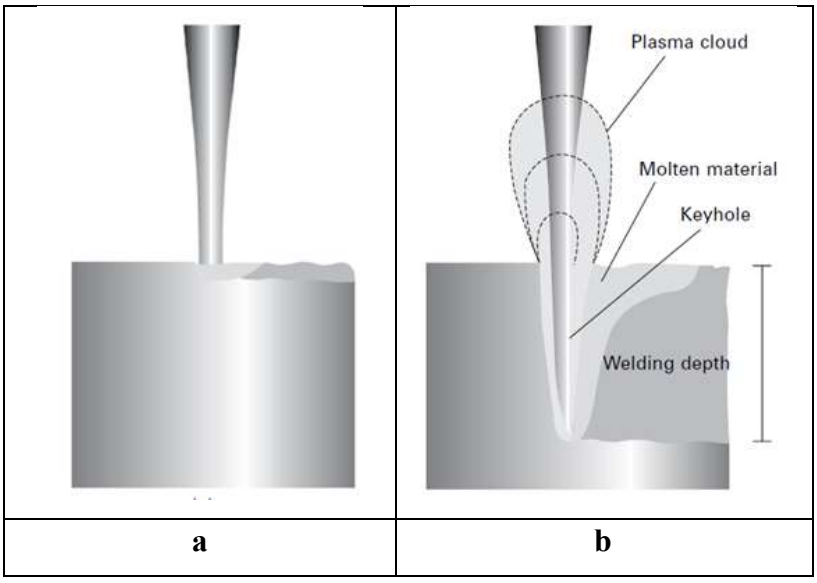

Figure 7: is a schematic representation of (a) conduction mode welding and (b) keyhole mode (deep penetration) welding [14].

One type of conduction mode weld is schematically illustrated in Figure 9-a. In the keyhole mode, as depicted in Figure 9-b, the input laser energy is so intense that it cannot be removed by conduction, convection, or radiation processes. Consequently, the portion of energy striking the workpiece causes melting and vaporization. The rapid evaporation of the metal forms a keyhole (a small-diameter cylindrical hole). As the keyhole deepens, the laser is periodically scattered inside it, increasing the laser energy absorption by the material. Vapor pressure within the keyhole prevents its collapse, consisting of molten metal walls [14].

The fundamental difference between these two modes is that in the first mode, the surface of the weld region is not broken, whereas in the keyhole welding mode, the surface of the weld region is opened to allow the laser beam to penetrate into the molten area. The conduction mode welding, due to the limited penetration of the laser into the material, results in less gas absorption during welding. In keyhole welding, the intermittent closure of the keyhole leads to the formation of a cavity in the weld. Conduction and keyhole welding modes can transition into each other during welding, depending on laser power, pulse width, and other parameters [14].

2-2-3 Types of Lasers Used in Welding

The types of lasers used in laser welding include CO_2 lasers and Nd:YAG lasers, which are primarily used in industrial applications. The Nd:YAG laser is a solid-state laser with a laser wavelength of approximately 1.06 μm. The excitation of the active medium can be continuous or pulsed (pulsed) in nature. In pulsed systems, a low-energy source is used, generating a high-energy pulse, where pulse parameters like duration and frequency play a significant role. CO_2 gas lasers are the most important gas lasers used in welding and cutting applications. These lasers utilize a gas mixture containing nitrogen, helium, and a small percentage of carbon dioxide (CO_2) and electrical discharge to pump the laser medium (excite CO_2 molecules).CO_2 lasers, in comparison to Nd:YAG lasers, have higher output power and efficiency, are more reliable, and are considered safer to work with. Nd:YAG lasers, with the development of their output power, improved laser beam quality, and the possibility of beam transmission via optical fibers, have entered fields that were previously dominated by CO_2 lasers. The shorter wavelength of Nd:YAG results in a higher percentage of laser energy being absorbed by the workpiece. Therefore, for the same penetration depth and equivalent speed, Nd:YAG lasers require lower power compared to CO_2 lasers. The wavelength of the beam fundamentally affects the absorption (amount of energy absorbed by the welded or cut metal) [15].

2-2-4 Principles of the Nd:YAG Laser Welding Process"

In this case, the laser material is a crystal containing garnet, aluminum, and yttrium, partially doped with neodymium (Nd). Figure 10 presents the general structure of the Nd:YAG laser welding process. As shown in Figure 10, a high-power lamp is used to excite the Nd atoms. A series of mirrors reflect the generated light onto a focusing lens, which concentrates the generated light at a focal point. The wavelength of the generated light is 1064 nm [15].

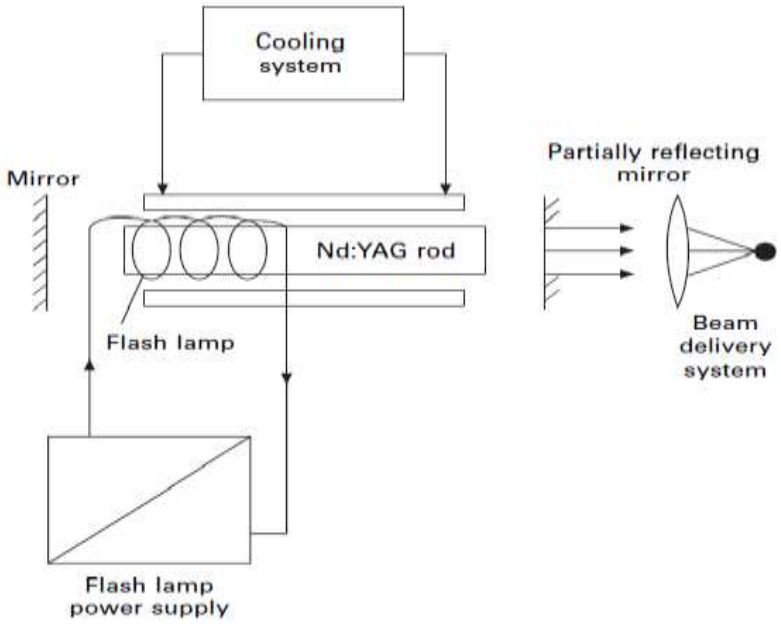

Figure 8: illustrates the general structure of the Nd:YAG laser welding process [15].

2-3 Residual Stress

2-3-1 Residual Stress Definition

Residual stresses (RS) refer to those types of stresses that remain in a material or body after the production and processing of materials in the absence of external forces or thermal gradients. Residual stresses are generated by loading during operation, leading to heterogeneous plastic deformation in the specimen or a part of it. These stresses can be macroscopic or micro stress and can exist in a component at any time. In Figure 9, parameters affected by residual stress are provided. Residual stresses can be classified as follows:

• Macrostresses (Type I Residual Stresses): These stresses are uniform across large regions and are nearly identical. They exist in individual grains of a material and within the entire material in equilibrium.

• Microstructural Residual Stresses (Type II Residual Stresses): These stresses are nearly uniform within microscopic regions, such as within a single grain or a part of a grain, and along several grains in equilibrium.

• Ultra-Microstructural Residual Stresses (Type III Residual Stresses): These stresses are nearly uniform within extremely small microscopic regions of a material, similar to each other. They exist over a few atomic spacing within a grain and along small portions of a grain in equilibrium.

Figure 9: shows the parameters affected by residual stress [16].

2-3-2 Various Sources of Residual Stresses

Residual stresses in metal structures arise for various reasons during the manufacturing process, such as rolling, forging, casting, and welding. These sources provide different types and levels of residual stresses. In some methods, the possibility of producing both compressive and tensile residual stresses in a specimen simultaneously exists. In welding, residual stresses result from thermal stresses and strains during the heating and cooling cycles in the weld zone and its vicinity [17].

2-3-2-1 Microscopic stresses

Microstresses are quantitative properties of a sample, such as yield percentage or hardness. They lack a specific direction and result from defects and imperfections within the crystal lattice. Microstresses are generated by internal strains within the crystal lattice, and their influence extends throughout the crystal's dimensions. These microstresses vary from one point to another within the crystal lattice, and

their effects can be observed as alterations in lattice parameters and broadening of X-ray diffraction peaks [17].

2-3-2-2 Sources of Microstresses Generation

Microstresses are generated due to non-uniform plastic deformation in small dimensions. For example, plastic deformation between the matrix and precipitate in a two-phase alloy creates microstresses within the matrix and around each precipitate. When an alloy consists of a matrix and a precipitate phase with different yield points, the deformation caused by the uniform force on the material, due to the different yield points of the matrix and precipitate, results in different levels of strain in these two phases. These differences, due to the solid and unyielding nature of interfaces, create microstresses at the precipitate-matrix interface to establish equilibrium between the matrix and precipitate. In some cases, microstresses can arise from the non-uniform distribution of elastic constants in materials. For example, two adjacent grains with different crystallographic orientations but the same elastic constants in a specific crystallographic direction may experience different strains due to the difference in crystallographic orientation. This leads to the application of stress at grain boundaries to limit the differential size change between the two grains and prevent the formation of voids at the grain boundaries. This type of stress is caused by the lack of elastic compatibility between two adjacent grains. It has been experimentally observed that in most multi-phase alloys composed of a matrix phase and several precipitate phases, the resulting microstress level extends over a larger region than just a few grains and represents a certain and averaged value. This type of stress is referred to as pseudo-macrostress, indicating the average microstress in a significant volume of grains. This average stress value is uniform within the desired phase region and is independent of the stress level present in the matrix or other phase regions [16].

2-3-2-3 Macroscopic stresses

Macroscopic stresses generate uniform strains that cause angular displacement of the diffraction peaks of X-rays. Macroscopic stresses are often generated during thermal or mechanical processes such as rolling, shot peening, and more, affecting a wide area of the component. In other words, inducing a uniform plastic deformation on a component leads to the generation of uniform residual stresses with a specific direction and magnitude in the region undergoing deformation. In general, sources of macroscopic residual stresses can be classified according to Table 5.

Table 4: sources of macroscopic residual stresses [16]

Mechanical Resources	Heat Sources	Chemical Resources	Composite Resources
Machining	Heating and Quenching	Oxidation and Corrosion	Powder Metallurgy
Shot Peening	Welding and Soldering	Plating and Coating	Surface Finishing Deficiency
Grinding	Final Heat Treatment Processes	Nitriding and Carburizing	Non-Thermal Phase Transformations
Forming Processes	Casting	-	Cavitation
Assembling	-	-	-

2-3-2-4 Thermal Resources

1- Induction Hardening
2- Heat Treatment and Quenching of Components
3- Ultra-Rapid Cooling in Laser Hardening
4- Casting
5- Laser Shot Peening
6- Welding and Soldering
7- Final Heat Treatment Processes
8- Distortion Due to Thermal Changes

2-3-3 Residual Stresses Resulting from Welding.

The creation of residual stresses can be explained through heating and cooling under constraint. Figure 10 depicts three similar metallic rods connected to two solid pieces. Initially, all three rods are at room temperature. Now, consider that the middle rod is heated, while the side rods prevent its thermal expansion, as shown in Figure 10-a. As a result, compressive stresses are generated in the middle rod, and these stresses increase with temperature until the yielding stress is reached. The yielding stress represents the highest stress limit in a material where plastic deformation begins. When the heating is

stopped, and the middle rod begins to cool down, the side rods continue to prevent its thermal contraction, as shown in Figure 10-b.

Consequently, the compressive stresses in the middle rod rapidly decrease and transform into tensile stresses. As the temperature decreases, these tensile stresses increase until they reach the tensile yielding stress. Therefore, residual tensile stresses, during cooling to room temperature, will be equivalent to the yield stress at room temperature in the middle rod. The residual stresses in the side rods will be of the compressive type and equivalent to half the tensile stress in the middle rod [18]. Residual stresses are generated in welding, even in the absence of phase changes in the solid state. The characteristics of these residual stresses in welded structures are described in terms of magnitude, direction, and partial distribution, collectively referred to as the field [18].

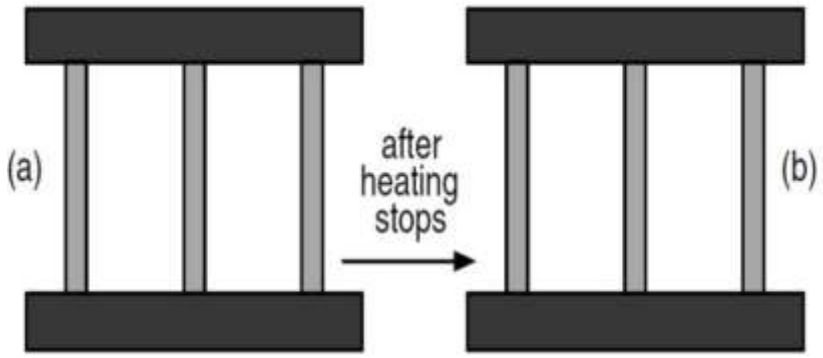

Figure 10: depicts the stresses resulting from heating, (a) during heating, and (b) during cooling [18].

The measurement and calculation of residual stresses typically exhibit a wide dispersion due to variations in the location of identification and measurement, measurement device or human errors, assumptions made in calculations, changes in material type, and other factors. Improving these measurements will require accurate data recording during production and service. Residual stresses before welding arise from mechanical or thermal processes. Among these processes, we can mention casting, forging, rolling, heat treatment operations, machining, and more. These stresses are sometimes removed or reinforced by each other until the welding stage. Therefore, when calculating the final residual stresses, these stresses should be considered. The best and simplest assumption in welding is that the maximum tensile residual stress equals the material's yield strength. After welding, processes such as creep, surface corrosion, applied loads, machining, and shot peening can alter the surface stresses [18].

Welding or soldering carries with it significant impacts, including:

- Creation of a significant amount of stress in the specimen known as residual stress.
- Impact on localized yield strength of components, depending on the sign and multiaxial nature of the residual stress.
- Formation of cracks without the presence of external loads.
- Increased likelihood of brittle fracture at points with maximum stress.
- Influence of the distribution of residual stresses on crack loading conditions.
- Strength and fatigue life.
- Elastic stability.
- Distortion of components.

In welding, stress is typically induced across the entire cross-section due to temperature changes, as shown in Figure 11. By observing and analyzing this diagram, it cannot be concluded that thermal stresses during welding are created by complex mechanisms involving plastic deformations over a wide range of temperatures, from ambient temperature to the melting point. However, to control residual stresses, factors such as input heat, consumable material in welding, supports and restraining effects, pre or post-weld heat treatment, section cooling, or vibrational effects during welding should be considered to reduce stress [19]. Additionally, the number of welding passes and their sequence also have an impact on applied stresses [20]. Figure 12 schematically illustrates changes in temperature (ΔT) and stress in the welding direction (σ_x) during welding.

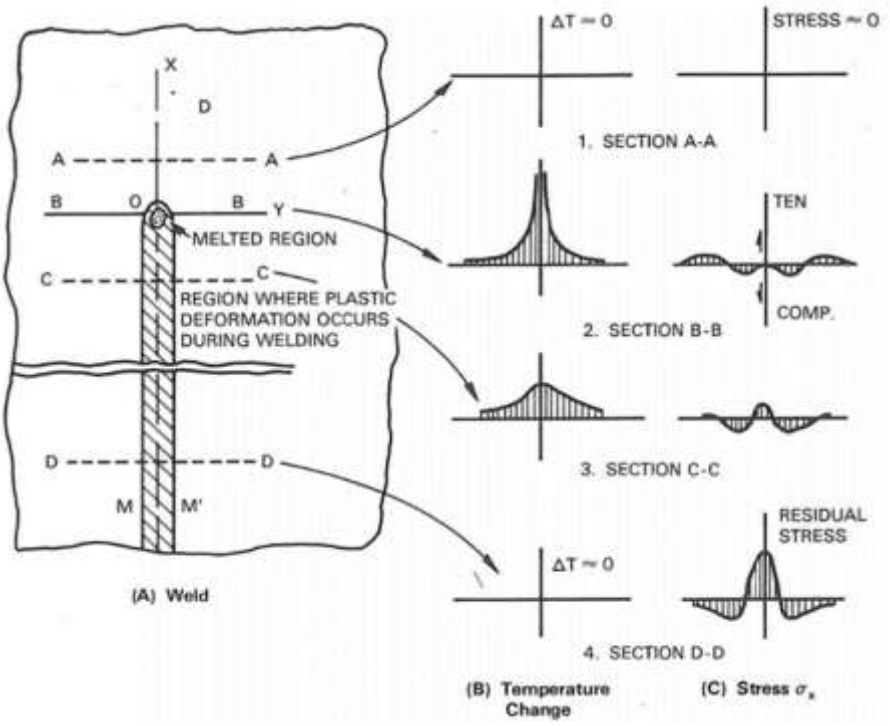

Figure 11: depicts the temperature and stress distribution across the flat weld cross-section [21].

The grooved region represents an area where plastic deformation has taken place. Section A-A is positioned ahead of the heat source and has not yet been significantly influenced by the input heat. Consequently, in this section, the temperature change caused by welding, ΔT, is negligible. Moving along section B-B, which intersects with the heat source, the temperature distribution exhibits a steep gradient. In section C-C, located at some distance behind the heat source, the temperature distribution has a gentler slope, and in section D-D, which is sufficiently distant from the heat source, the temperature remains uniform. Now, let's consider the thermal stresses in the longitudinal direction, denoted as σx.

Due to the fact that section A-A has not been influenced by the input heat, бx is equal to zero in this area. Along section B-B, бx is close to zero in the regions under the heat source. The reason for this is that the weld pool lacks the strength to withstand a significant load. Further away from the heat source, stresses become compressive (with negative бx) because the expansion of these regions is controlled by the metal at lower temperatures around them. Due to the low yield strength of the metal at high temperatures in these regions, бx approaches the yield strength of the base metal at this temperature. In areas further away from the weld, бx is tensile and balances with compressive stresses in the regions near the weld. Along section C-C, both the weld metal and the adjacent base metal have cooled down,

and therefore, they tend to contract, resulting in tensile stresses (бx is positive). In the regions near the weld, бx is compressive.

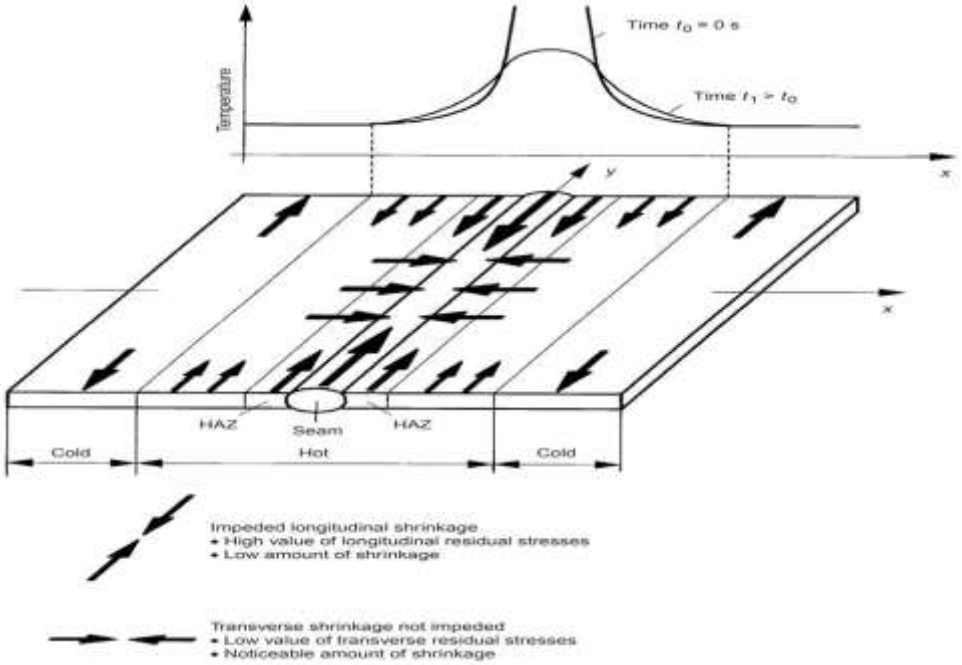

Figure 12: is a schematic representation of contraction resulting from the heterogeneity of the heat distribution [21].

Finally, along section D-D, the weld metal and the nearby regions of the base metal have cooled down and contracted. As a result, more tensile stresses are created in the areas near the weld and compressive stresses in the regions further away from the weld. Because section D-D is entirely behind the heat source, the stress distribution beyond it does not change significantly, making the stress distribution a residual stress distribution [21]. Residual stresses result from heterogeneous elastic and plastic deformations, as depicted in Figure 14, appearing on both macro and micro scales.

These deformations in welding within the weld bead itself or the Heat-Affected Zone (HAZ) are a result of the distribution of heat and temperature. The manner in which heating occurs is also an important parameter in the distribution of residual stresses, and by adhering to an appropriate preheating pattern, these stresses can be minimized. When two fused metals are of the same type, the final structure in the weld metal within the HAZ region is symmetrical, and this symmetry also exists in the distribution of residual stresses. However, when two different materials are used, the distribution

of residual stresses will not have symmetry due to the existing microstructure and physical properties. In this case, the softer metal will tend to eliminate some of the generated stresses [22].

2-3-4 Types of Stresses Resulting from the Welding Process

In the welding process, residual stresses originate from various sources, with the most important ones listed below:

A) Residual Stresses Due to Contraction: Some of the stresses in a welded specimen result from contraction. This type of stress occurs when hot and cold regions are adjacent to each other. The level of contraction strongly depends on the coefficient of thermal expansion and the rate of heat dissipation from the specimen. If tensile thermal stresses occur during cooling and these stresses exceed the material's yield strength, they will remain as residual tensile stresses after solidification. In regions where melting does not occur, thermal strains occur in a compressive manner and when they exceed the yield strength, they create residual compressive stresses. In some cases, these stresses can be tensile and result from thermal contraction of the metal. This level of contraction will be entirely counteracted by the expansion resulting from initial heating. Figure 13 illustrates how the distribution of residual stresses changes in the cross-section, confirming the mentioned information [16].

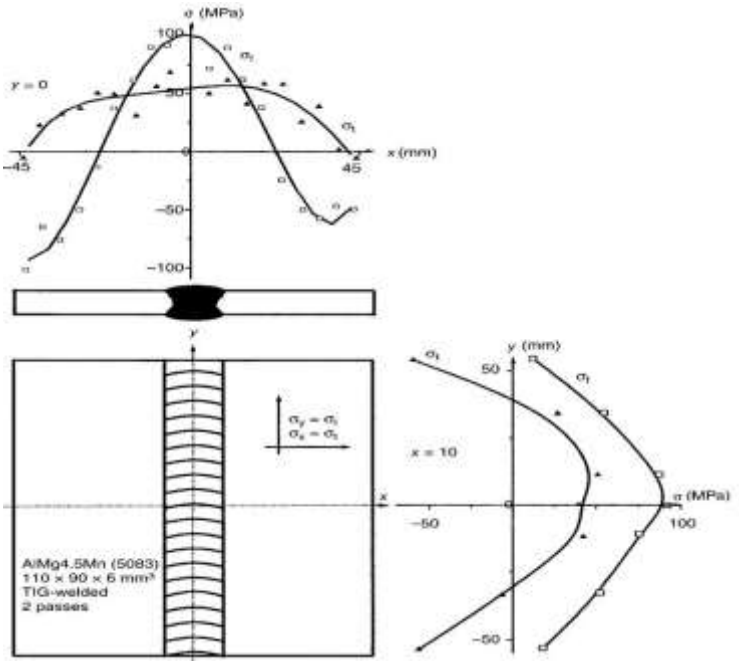

Figure 13: Distribution of Residual Stresses in Different Directions in a Welded Aluminum Plate with Two Passes by the TIG Process [16].

B) **Residual Stresses Due to Quenching**: If the specimen is thick, it will generally experience compressive stresses at the surface and tensile stresses in the depth as it cools. If these stresses exceed the yield limit, they will result in residual stresses and heterogeneous plastic deformations.

C) Residual Stresses Due to Phase Transformation: Residual stresses arising from phase transformations during the cooling of the molten zone in welding are among the most significant sources of heterogeneous residual stresses. This heterogeneity can be attributed to variations in maximum welding temperatures, differences in cooling rates, and slight alterations in chemical composition. In the case of steel, the transformation of austenite into ferrite, pearlite, and martensite results in an increase in volume and the generation of compressive residual stresses. However, this pattern is not fixed, and the direction of residual stresses depends on cooling rates and contractions. Figure 16 illustrates the regions where phase transformations occur. Cooling from elevated temperatures induces contraction in the specimen. The onset of austenite transformation into pearlite and ferrite is associated with reduced tensile residual stresses. Over time, this transformation reaches its maximum compressive strength, which is the yield strength under compression. Subsequently, as the material continues to cool, contraction persists, ultimately leading to the presence of tensile yield stresses. In cycles 2 and 3, the formation of bainite and martensite becomes evident. During these cycles, due to the specific cooling conditions, yield strength and compressive stresses can develop to higher levels and temperatures, resulting in the persistence of compressive residual stresses at the end [16]**.**

In Figure 14, the influence of heating rate is depicted schematically. It is evident that when the heating rate decreases from 1 (Tt high) to 4 (Tt low), the remaining stresses are in a compressive state and transition to tensile as the temperature increases. As illustrated in Figure 16, in curve 3, which takes on a W shape, the residual stresses are a result of the rate and magnitude of low input heat and the transformations that occur. However, in curve number 2, the residual stresses are primarily compressive, increasing with higher input heat, and are mainly confined to the Heat Affected Zone (HAZ), with maximum tensile residual stresses in the weld nugget.

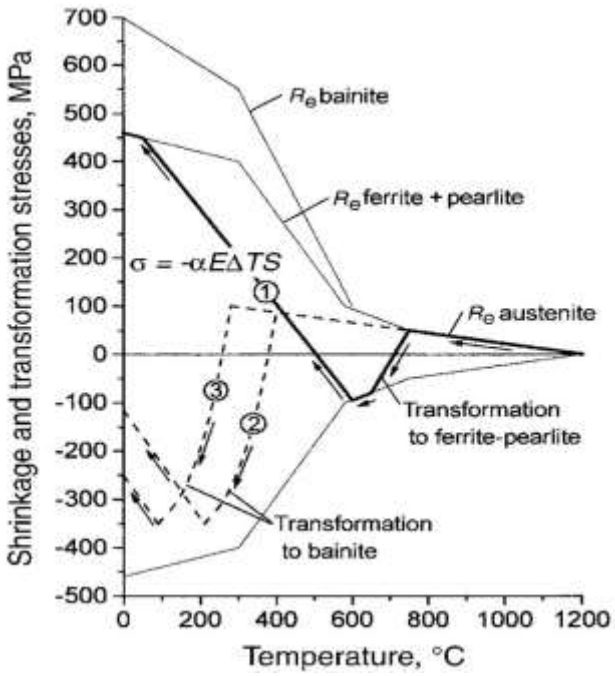

Figure 14: depicts residual stresses resulting from contraction and phase transformation with temperature variations [16].

In summary, welding-induced stresses result from three distinct processes:

• Thermal expansion and contraction due to temperature gradients.

• Quenching effect.

• Phase transformation.

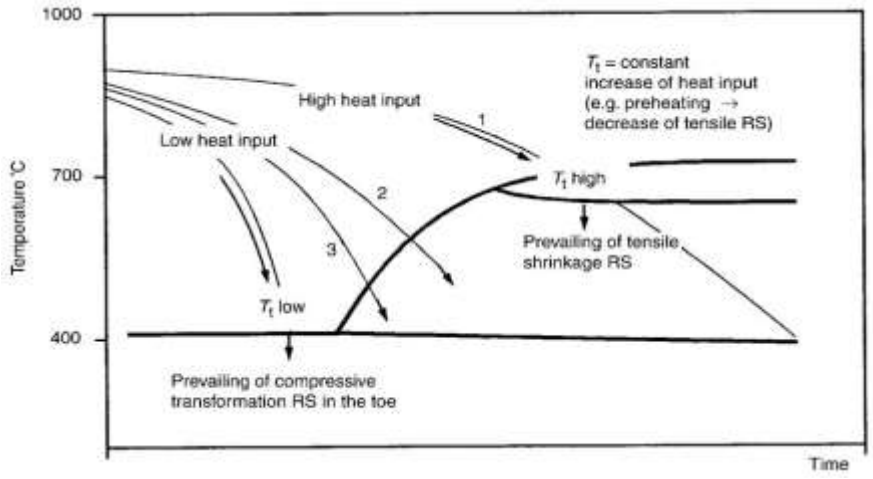

Figure 15: illustrates the effect of input heat on the phases and resulting contractions [16].

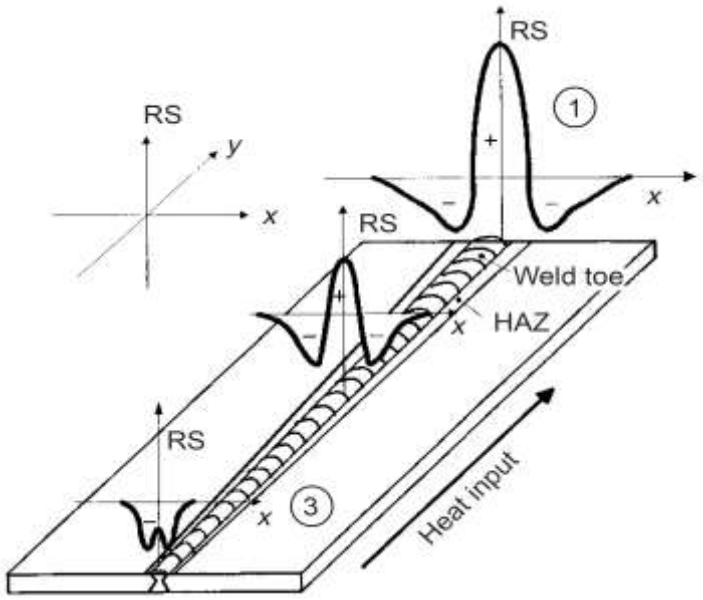

Figure 16: illustrates the influence of input heat on the distribution of residual stresses in the weld nugget [26].

2-4 Methods of Residual Stress Measurement

In recent decades, various quantitative and qualitative methods for analyzing residual stress have been developed. Generally, a distinction has been made between destructive and non-destructive methods for measuring residual stress. Different methods for determining residual stresses are classified into three groups: destructive, semi-destructive, and non-destructive. Table (2-8) illustrates the categorization of these methods.

Table 5: Classification of Residual Stress Measurement Methods [23].

Non-destructive	Semi-destructive	Destructive
X-ray diffraction	Drilling	Contour
Neutron diffraction	Ring-core	Sectioning
Ultrasonic	Deep hole	Crack removal
Barkhausen noise	Magnetic particle	Layer removal

2-4-1 Destructive Methods for Measuring Residual Stress

All mechanical (destructive) methods for measuring residual stress require measuring the strain changes resulting from the release of residual stress, which are calculated based on the linear elasticity laws. In all of these methods, various techniques are used to access a depth from the surface and measure the strain resulting from the released stress using a strain gauge. Finally, the measured strain is converted to stress using specific relationships. The use of these destructive methods depends on factors such as availability, cost, and required accuracy and is primarily limited to laboratory samples.

2-4-2 Semi-destructive methods for measuring residual stress

Semi-destructive methods, although they involve minimal damage to a sample, are not used for components with sensitive applications, especially in aerospace and marine industries.

2-4-3 Non-destructive methods for measuring residual stress

The third group of residual stress measurement methods is based on the relationship between physical parameters and crystallography and does not require the destruction of the entire or part of the structural elements. Therefore, they can be used for background measurements [42].

The most important developed non-destructive methods include:

• X-ray and neutron diffraction methods: These techniques rely on measuring lattice spacing based on strain scales. They allow for the investigation and differentiation of three types of residual stresses. Currently, X-ray diffraction is the most widely used non-destructive method for assessing residual stress.

• Ultrasonic methods: These approaches are based on alterations in the velocity of ultrasonic waves within materials subjected to mechanical stress.

• Magnetic methods: These methodologies depend on the interplay between magnetization and elastic strain in ferromagnetic materials. Various magnetic properties, such as permeability, magnetization, residual magnetism, and Barkhausen noise, can be examined

2-5 Expected Criteria for Stress Relaxation Measurement Methods

The presence of residual stresses in the weld cross-section due to their mechanical effects necessitates the development of various methods to identify and estimate these stresses. Initially, it is essential to focus on the objectives and expectations regarding the determination of residual stresses. In this regard, one should consider what expectations should be associated with a method,

regardless of its type and efficiency, and how to judge its usefulness or superiority compared to other methods. In this context, five aspects should be taken into account when examining and analyzing the final results [19]:

A) Destructive Test Severity: The foremost criterion in test classification pertains to the extent to which conducting the test will result in specimen destruction or introduce consequential side effects. In essence, it assesses how far the test will go in terms of causing the sample's damage, and, at times, even its obliteration. Of utmost importance is the consideration of how these effects might give rise to supplementary stresses, thereby influencing the ultimate outcome's precision? This viewpoint holds substantial significance, as it serves as the basis for categorizing various methods employed to identify residual stresses into three distinct groups: destructive, semi-destructive, and non-destructive. For instance, in semi-destructive techniques like strain gauging through hole-drilling, there may be a requirement to remove or excise a layer or segment of the material to alleviate and compute the stress. However, this procedure, aside from bringing about physical alterations, can potentially induce thermal or mechanical stresses within the welded sample, thereby impacting the result's accuracy. Even in non-destructive methods, such as ultrasonic testing, where surface grinding of the weld is necessary for optimal sensor installation, it can result in the imposition of additional tensile residual stresses on the sample's surface [19]

B) Resolution Level: This parameter is contingent on the surface, depth, or volume of the weld specimen that needs stress measurement and presentation as the final results. As the resolution level of a measurement method decreases, it typically involves calculating the average stresses within larger portions of the weld and may fail to report critical higher stresses due to this averaging effect. Therefore, variations in results among different measurement methods with varying resolution levels hinder direct comparison between them [19].

C) Measurement Depth and Penetration: In many methods for determining residual stresses, stress measurements will be displayed at or beneath the weld surface. Nevertheless, the depth at which stresses exist often needs to be determined non-destructively.

d) Stress Directions: Residual stresses are tensor quantities. The stress tensor is symmetric and consists of a 3x3 matrix. However, each method may report stress magnitude in a specific direction (which may not necessarily be along the principal axes) as a scalar value. Therefore, it may not provide extensive information for the analysis of the stress tensor.

E) Cost: The cost of conducting tests is also a limiting factor. Economic and financial justification is essential, especially when expecting a method to gain popularity and industrial application. It

must have economic viability. However, other factors such as the transportability of equipment and their usability in different conditions, as well as the speed of conducting tests, can also be influential. Nevertheless, during research work, these reasons may not be as crucial.

Hui Huang et al. [24] were studied on High performance computation of residual stress and distortion in laser welded 301L stainless sheets. X-ray diffraction (XRD) and contour method were used to measure the surficial and internal residual stress respectively. They found that these heat effects must be taken into account for accurate prediction of residual stresses in laser welded stainless sheets. Reasonable agreement among residual stresses by numerical method, XRD and contour method was obtained. Buckling type welding distortion was also well reproduced by the developed thermo-mechanical FEM.

Based on numerical results and experimental measurement, the following conclusion were drawn:

The welding numerical model can be separated in weakly and strongly nonlinear regions, and these regions can be solved iteratively. Furthermore, the mesh density can be made different for the regions so that the model can be represented with minimum number of DOFs. Through numerical analysis of laser welding problem over 50,000 elements, the hybrid iterative substructure and multi-level refining method shows superior computing performance over commercial code ABAQUS. The mesh refinement can be easily achieved and solution accuracy is guaranteed. Accuracy of residual stress calculation in stainless steel depends on strain hardening, annealing and melting effects. It is necessary to limit the increase of plastic strain at high temperature and initialize the accumulated plastic strain in the weld pool. Numerical model with these considerations predicted reasonable residual stresses distribution [24].

The welding residual stresses in thin stainless sheets were successfully measured by contour method. The obtained stress profile has good agreement with that by X-ray diffraction method. The thermal-mechanical analysis of laser welding model with million order DOFs can be solved by proposed numerical method in several hours. The welding distortion of thin sheets are well reproduced in mode and magnitude [24].

Tadamalle et al. [25] were investigated the evaluation of distortion and residual stresses in dissimilar metal laser welds. The objective of this research work is to evaluate distortion and residual stresses induced in dissimilar metal butt weld joints. The 304 L stainless steel and mild steel sheets of 0.98 mm thick are used in automobile industries.

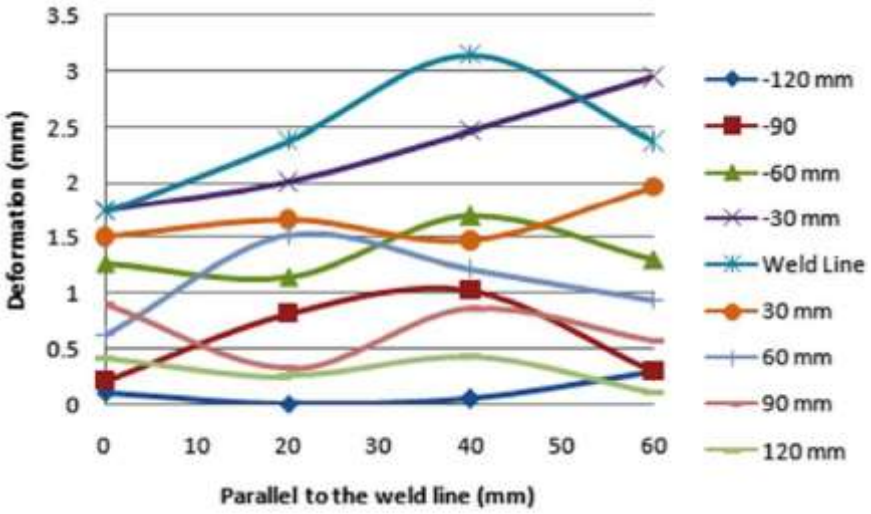

Figure 17: Distortion measured in the transverse direction to the weld centerline [25].

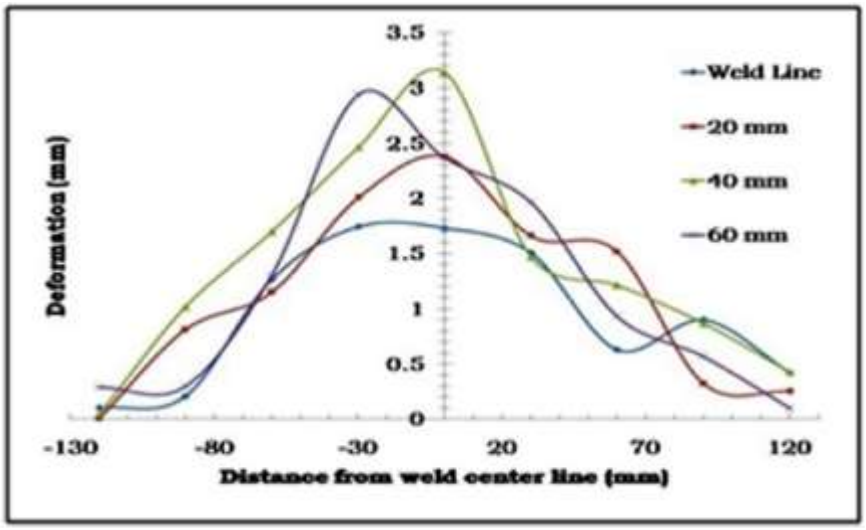

Figure 18: Distortion measured parallel to the weld line [25].

Yan et al. [26] studied on Prediction of temperature field and residual stress of oscillation laser welding of 316LN stainless steel. To study the effect of oscillation parameters on the temperature field and residual stress. Firstly, the welding experiments of the oscillation laser beam with different oscillation tracks and the fixed frequency of 100 Hz and the fixed amplitude of 2 mm are respectively performed. The top surface and the cross-section geometry morphology of the welding pieces as shown in Figures 19 and 20, respectively. The weld pool presents severe spatter when the oscillation trajectory of laser beam is no oscillation and '8′ and '∞', and the oscillation trajectory of laser beam parallel with the

welding direction produces the WM with the nonuniform weld width. At the same time, the oscillation trajectory of '8′ and 'circle' and '∞' present the severe undercut defection due to the oscillation of laser beam cause the excess energy to radiate on both sides of WM.

The no oscillation moving and the parallel oscillation are prone to produce pores due to the collapse of keyhole results in the bubbles difficultly overflow from the weld pool of large the ratio of depth to width. When the laser beam executes the oscillation moving, the deep penetration welding gradually transits to the heat conduction welding. The width of WM of oscillation welding is larger than that of the laser beam without no oscillation moving, oppositely, the penetration depth of WM of oscillation welding is smaller because the oscillation motion vertical to welding direction increases the radiated area of BM, which disperses the energy of laser beam, which is same as the viewpoint of Jiang et al. [27].

According to the requirements of technology, considering the geometry morphology and defection of WM, and the vertical oscillation is selected as the oscillation pattern of oscillation laser beam welding to optimize the process parameters.

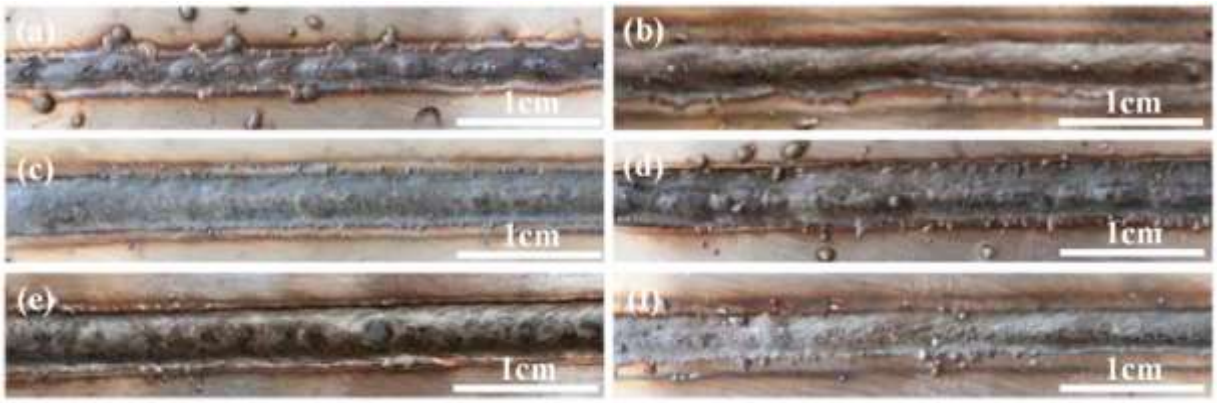

Figure 19: Top surface of 316LN WM with different oscillation track; (a) no oscillation, (b) parallel oscillation, (c) vertical oscillation, (d) 8, (e)circle oscillation, (f) ∞ [26].

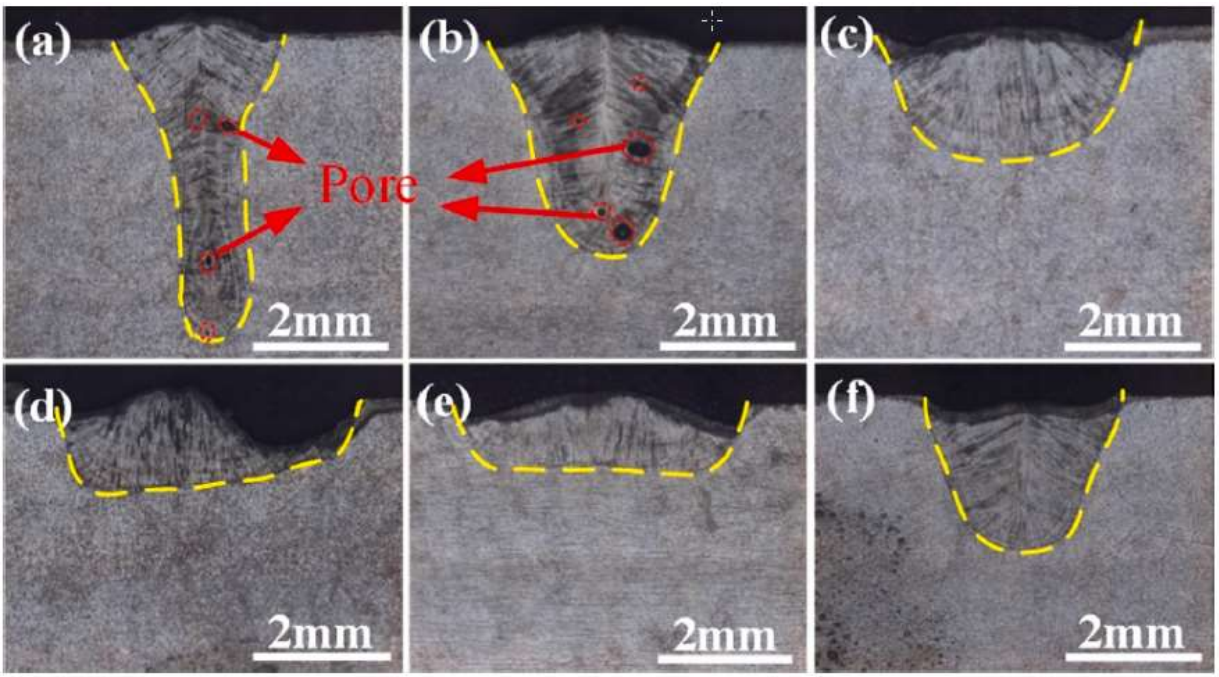

Figure 20: Cross section morphology of WM with different oscillation track; (a) no oscillation, (b) parallel oscillation, (c) vertical oscillation, (d) 8, (e)circle oscillation, (f) ∞ [26].

The oscillation frequency of oscillation welding is an important factor influences the geometry morphology of WM. The top surface and cross-section morphology of different frequency weldments as shown in Figure 21. It can be seen that the too low oscillation frequency preferentially produces the WM with the characteristic of zigzag because the fusion zone after the laser beam scanning is not completely superposed. The fusion line gradually verges to straight with the increase of frequency, which attributes to the continuation of energy distribution on both sides of WM, but the excessive oscillation frequency reduces the depth of WM, the literature [28] also has a similar experiment phenomenon.

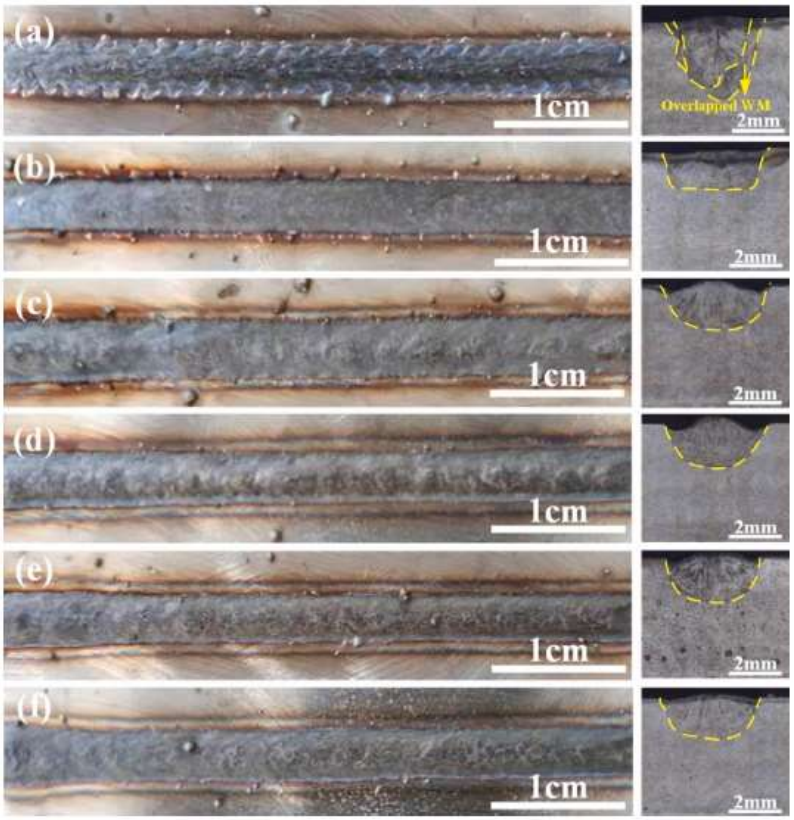

Figure 21: Geometry morphology of 316LN WM with different frequency; (a) 10 Hz, (b) 30 Hz, (c) 50 Hz, (d) 100 Hz, (e) 150 Hz, (f) 200 Hz [26].

The amplitude of the oscillation laser beam is another important parameter significantly influences the geometrical morphology of joints. So the laser welding experiments of the different oscillation amplitudes and the fixed frequency of 100 Hz and vertical oscillation pattern are conducted. The top surface and section cross morphology are shown in Figure 22. The top surface of WM of 0.5 mm and 1 mm amplitude presents in a lot of patter particles and the patter phenomenon gradually is alleviated with the increase of amplitude. With the increase of amplitude, the depth to width ratio decreases, and the deep penetration welding gradually transforms to the heat conducted welding because the laser beam radiated on the surface area of substrate increases, which results in the laser energy is dispersed and unfocused. However, the penetration width of 1 mm amplitude obviously declines in Figure 22, which may be the inappropriate position of welded-sample is selected to observe. It can be seen that the pores present in WM zone of 0.5 mm amplitude due to the bubbles difficultly flee from the weld pool of large depth to width ratio.

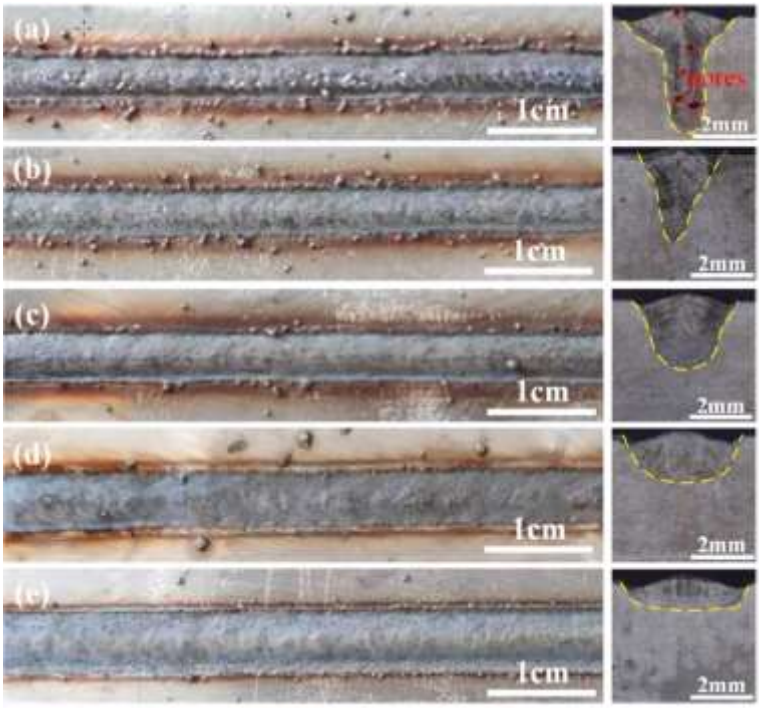

Figure 22: Macro-morphology of 316LN WM with different amplitudes; (a) 0.5 mm, (b) 1 mm, (c) 1.5 mm, (d) 2 mm, (e) 2.5 mm [26].

Yan et al. [29] studied on Prediction of temperature field and residual stress of oscillation laser welding of 316L stainless steel. The transverse (σx) and longitudinal (σz) residual stress distribution of different amplitudes are calculated along the red dash line of Figure 23-a, the results are denoted in Figure 23-b2 and c2, respectively. As seen in Figure 23 (b1) and (b2), it presents the transverse residual stress, the maximum transverse compressive stress on the center of the surface of the weldments reaches about 90.9 Mpa when the amplitude is 0.5 mm. As the increase of distance away from the center of FZ, the transverse compressive stress changes into the tensile transverse stress of which the maximum value is 143Mpa.

At the same time, the compressive transverse stress gradually reduces with the increase of the amplitude, eventually, the compressive transverse stress transforms to the tensile transverse stress of which the maximum value is 14 Mpa as seen in Figure 23 (b2). Fig. 24 (c1) and (c2) indicate the longitudinal residual stress distribution. The FZ and the surrounding material have the high longitudinal tensile stress results from the shrinkage of the weld pool during the solidification and the surrounding zone resists shrinkage so that the longitudinal tensile stress is formed in the WM and the nearby WM as the explanation of the literature [33].

As seen in Figure 24 (c2), the peak value of longitudinal stress of oscillation amplitude in the range from 0.5 mm to 1.5 mm is approximately equal, and the longitudinal peak stress concentrate in the narrow zone. The longitudinal stress is concentrated in the wider zone when the amplitude is greater than 2 mm, which attributes to the energy to disperse wider zone, and the higher peak temperature transfer to both sides of the laser beam radiated zone in Figure 25 (b), which effect can influence the type and magnitude residual stress, and the Ahmed et. al. [34] also proved the temperature gradient and the cooling speed can influence the distribution the residual stress.

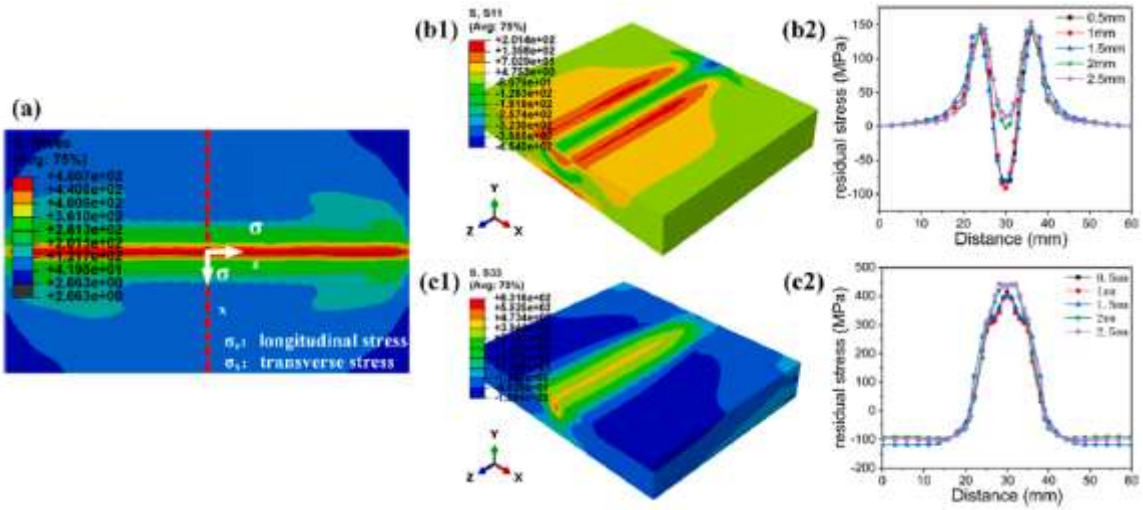

Figure 23: Residual stress distribution under the different amplitudes, (a) Von Mises equivalent stress distribution of 0.5 mm, (b1) transverse residual stress of 0.5 mm, (b2) transverse residual stress of the different amplitude, (c1) the longitudinal residual stress of 0.5 mm, (b2) longitudinal residual stress of the different amplitude [29].

The numerical as-weld distortion results of different amplitudes as shown in Figure 26. It can be seen that the distortion presents the decrease trend with the amplitude increases. According to the finite element model to optimize the welding parameters and alleviate the residual stress concentration and as-weld distortion, moreover, the optimization parameters are adopted to perform the oscillation laser TIG hybrid welding researches of more 10 mm thickness plate in the further [29].

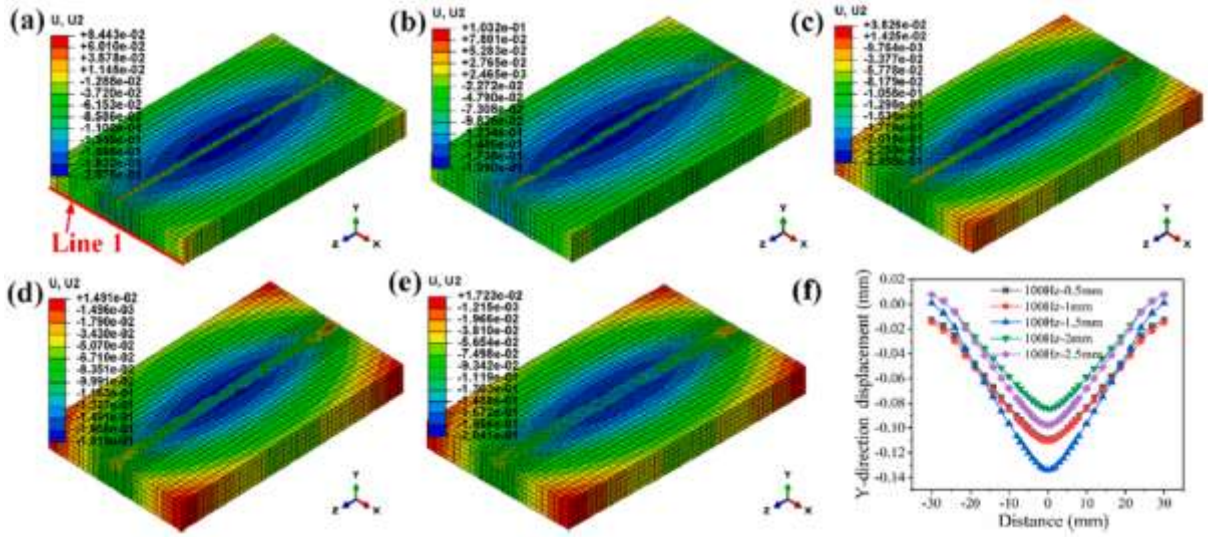

Figure 24: As-welded distortion under the different amplitude, (a) 0.5 mm, (b) 1 mm, (c) 1.5 mm, (d) 2 mm, (e) 2.5 mm, (f) Y-direction displacements along line1 of Fig. 11 (a) [29].

F. Giudice and A. Sili [30] were investigated the A theoretical approach to the residual stress assessment based on thermal field evaluation in laser beam welding. The experimental measurements were obtained at four points, positioned according to the scheme shown in Figure 27. The results of the experimental investigation show a good agreement with the theoretical construction of the distribution, with deviations in the values of the residual stresses within 7%, compared to the corresponding theoretical values. The experimental value detected at point P1 only is an exception. While in fact the points P2, P3, P4 (with distance from the welding line y = 16, 18, 21 mm, respectively) are subject to stress states that do not exceed the accuracy limit of the experimental technique (70% of the yield strength, i.e. 175 MPa) [31], the point P1 (y = 13 mm) is well beyond this limit.

According the theoretical construction, the yield point is reached at P1, and therefore, the stress state strongly deviates from the linear-elastic behavior assumed as one of the basic conditions in the calculation of residual stresses using the hole-drilling method. This deviation leads to larger margins of error in the experimental measurement, which has been estimated as positive and in the range 10 ÷ 30% for thick sections where blind holes are used [32]. The deviation between experimental and theoretical data estimated for point P1, equal to 16.2%, falls within this range, confirming that the residual stress at y = 13 mm exceeds the proportional limit and enters the yield field, in agreement with the theoretical construction of the stress distribution.

They found that two different modes have been defined to use the analysis of the thermal field due to laser beam welding for the theoretical calculation of the distribution of the longitudinal residual stresses. The first one makes use of a simplified formula well-known in the literature, which describes this distribution as a function of two fundamental parameters: the value of the distance b from the welding axis for which the residual longitudinal stresses reverse their sign (tension–compression), and the yield strength of the base metal at room temperature. In this case the simulation of the thermal field allows to calculate with precision the value of the parameter b, but the approach shows substantial limitations in the stress distribution modeling it provides. The second mode, which is based on a combined processing of thermal profiles and heating–cooling cycles, allows a full characterization of the longitudinal residual tensile stresses, obtaining results more detailed and compliant to the known distribution trends reported in the literature. A comparison of these results with the ones obtained by experimental measurements confirms the reliability and greater accuracy of the second approach to the theoretical calculation of residual stresses.

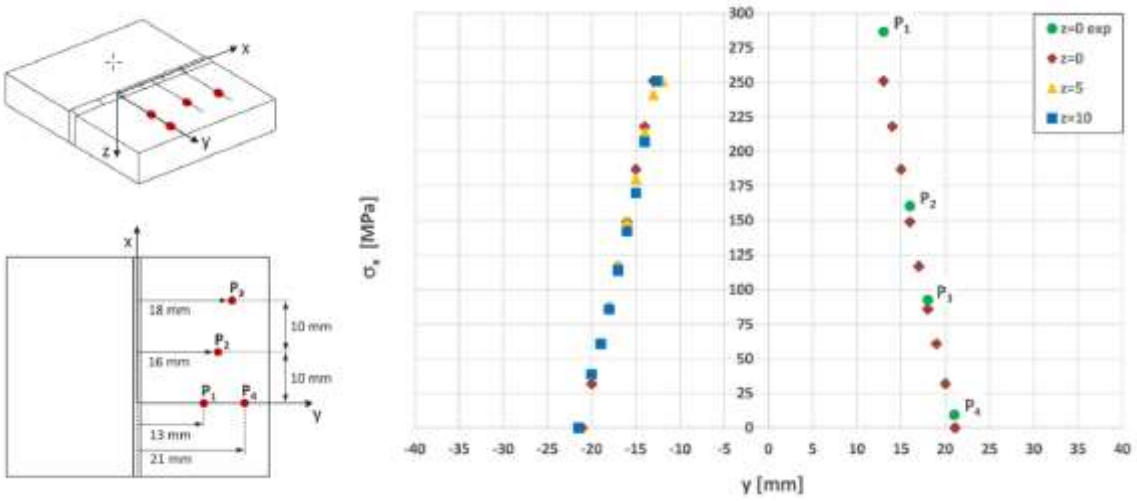

Figure 25: Residual stresses calculation by thermal field analysis and experimental validation: residual stress distributions as the depth z varies along the thickness of the plates (left side of the graph), and comparison with experimentally-measured stresses for z = 0 mm (right side of the graph) [30].

Zhng et. Al. [33] studied on the residual stress, micro-hardness and tensile properties of ANSI 304 stainless steel thick sheet by fiber laser welding. The fiber laser was chosen to weld the ANSI 304 stainless steel (ANSI 304SS) sheets with at thickness of 5 mm, and effects of laser power, defocusing distance and welding speed on the weld appearances were investigated. Residual stress, micro-hardness and tensile properties of laser welds and the base metal were characterized and analyzed compared with the conventional laser (CO_2, Nd: YAG) welding methods. The following conclusions

have been made: By the orthogonal test and the analyses on the appearances and properties of the fiber laser welds, the most appropriate welding parameter combination has been obtained, and it is described as follows: the laser powers 4000W, the defocusing distance is 3 mm and the welding speed is 35 mm/s [33].

Figure 26 shows the true stress–strain curves of the base metal and the fiber laser weld at the fixed welding parameters, CO_2 and Nd: YAG laser welds. Compared with the CO_2 and Nd: YAG laser welds, tensile residual stresses of the fiber laser weld are the lowest, micro- hardness and tensile strength are the highest. The crystal solidification process induced by the fiber laser welding is schematically illustrated and systematically revealed. The crystal solidified microstructure of the welding zone is completely different from that of the base metal. The middle of the laser welding zone can be considered as the demarcation line, and the crystal solidified microstructure grew with different orientations from either side of the demarcation line [33].

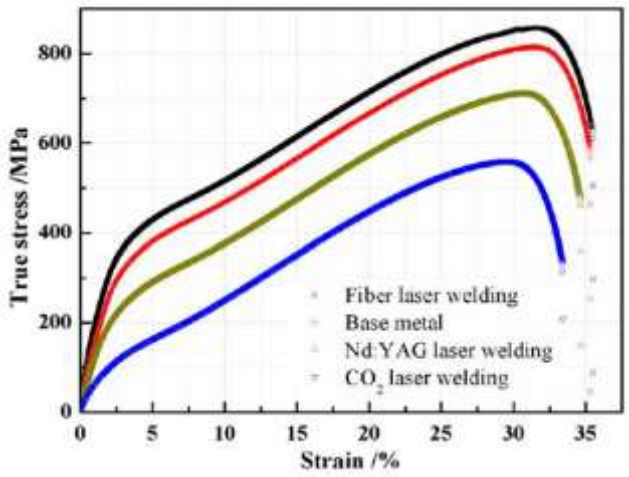

Figure 26: True stress–strain curves of the base metal and the fiber laser weld at the fixed welding parameters, CO_2 and Nd: YAG laser weld [33].

Gue et al. [34] investigated the residual stress distributions in laser and gas-metal-arc welded high-strength steel plates. They found that in GMAW and laser welding of S700 steel, solid state phase transformations have noticeable effects on the longitudinal residual stress distributions in the vicinity of the weld, through promoting an 'M' shaped residual stress distribution. This contrasts with a typical profile for a non-transforming material, where a single tensile peak would be expected at or near to the weld centerline. In the case where a single pass keyhole weld is made, such as with ALW, the 'M'

shaped residual stress distribution is likely to appear through the thickness of the plate being welded. If, however, a multi-pass welding technique is applied the 'M' shaped residual stress distribution is less likely to be present through the entire plate thickness. The peak residual stresses in GMAW and laser welds in S700 steel tend to arise to either side of the weld centerline, coinciding approximately with the HAZ–BM interface. The magnitude of the peak stresses appears to be in the order of the yield stress of the parent steel (~700 MPa), but can be somewhat higher due to the formation of strong, hard phases within the weld FZ and heat-affected zone. (4) The extent of the tensile regions appears to correlate with the extent of the metallurgical zones in the welds produced with each process. As such, the GMAW specimen exhibited tensile stresses over a wider region than both the ALW and ultra-NGLW specimens. The ultra-NGLW specimen, owing to its low heat input, produced the narrowest regions of tensile stress [34].

There are significant benefits associated with choosing a laser-based welding process over GMAW for the welding of S700 steel. These include the fact that the extent of softening in the heat-affected zone is significantly reduced through using a laser-based process. In addition, laser-based welding processes offer significant productivity gains, since the travel speeds are lower with GMAW and a greater number of weld passes is required for a joint of the same thickness. The consumption of filler material is also greatly reduced in the case of ultra-NGLW, or eliminated altogether in the case of single pass ALW [34].

Residual stress profiles measured by XRD at the mid-length position and on the top surfaces of the welded S700 steel plates are shown in Figure 27. The residual stresses induced by laser-based welding processes may be significantly higher than those associated with GMAW when they are applied to high strength steels, since laser-based processes tend to be associated with steeper temperature gradients, faster cooling rates, and hence a greater likelihood of increasing the yield stress of the material in the vicinity of the weld [34].

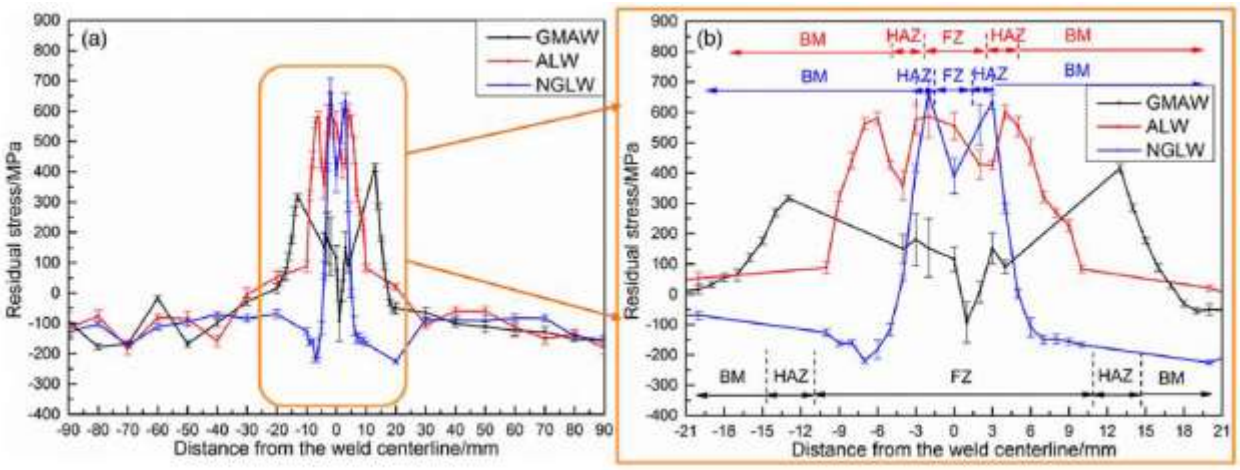

Figure 27: Residual stress profiles measured by XRD at the mid-length position and on the top surfaces of the welded S700 steel plates, (a) residual stresses as a function of distance from the weld centreline, (b) magnified residual stress profiles in the vicinity of the FZ and HAZ. Within the weld FZ, measured data were omitted if the measurement point coincided with a point on the surface that was far from flat [34].

Colegrove et al. [35] investigated the welding process impact on residual stress and distortion. The longitudinal residual stresses across the six welds are shown in Figure 28-a and 28-b comparison of the weld region with the model predictions is shown in Figure 28-b. The results indicate that the width of the tensile peak increases with heat input, as expected. Note however that the residual stress of the CMT and pulsed gas metal arc welding process are almost identical, indicating comparable (absorbed) heat input for the two processes. The comparison between the model and experimental predictions in Figure 30-b is particularly interesting. Although the magnitude of the peak stresses is not well represented by the model, there is remarkably good agreement in the width of the tensile stress regime. This result is pleasing given the simplifying assumptions made in the model. The magnitude of the tensile peak produced by the model is primarily a function of the yield tensile stress versus temperature data. Since this was not measured for the material used in the experiment it is hardly surprising that there is a discrepancy. In addition, there is very little variation in the peak residual stress between the processes, unlike the model predictions [35].

In particular, the measured residual stress for the laser weld is slightly lower than the other processes and does not appear to be affected by microstructural hardening. It is unclear why this should be the case, although there was relatively large point-to-point scatter in the residual stress data for the laser weld. The AWL calculated by the model increased with the heat input primarily due to a widening of the tensile residual stress region. There was a direct link between the AWL predicted by the model and

the distortion index, confirming previously published numerical results. Also there is good agreement between the width of the longitudinal residual stresses predicted by the model and those measured experimentally. However, the model fails to predict the peak residual stress values correctly which is primarily due to poor yield stress versus temperature data used in the model [35].

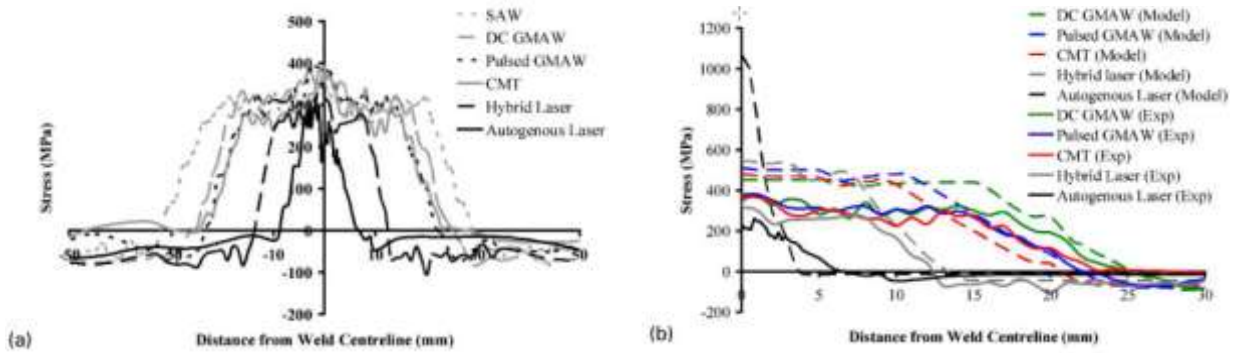

Figure 28: (a) longitudinal residual stress measured across six samples, (b) comparison with model predictions [35].

Costa et al. [36] studied on the experimental results and numerical predictions of the residual stresses in joints manufactured with two hot-working tool steels: X.40.CrMoV.5.1 and 40.CrMnNiM-o.8.6.4, in the laser-deposited layer and in the heat-affected zone. Figure 29 shows the residual stress distribution at material' surface, in longitudinal and cross directions, of P20 steel specimens. Trough-depth residual stresses evaluation after laser deposit welding were performed in order to analyses the influence of the residual stress state on fatigue behavior of mound steels. Both X-ray diffraction sin 2c method (XRD) and incremental hole-drilling technique (IHD) were used in residual stress measurement. The reported that Residual stresses induced by laser deposit welding were evaluated by incremental hole-drilling (IHD) and X-ray diffraction (XRD). Surface residual stress distribution, as well as through the thickness residual stresses at the center of the small weld seam, were determined. Coherent and reproducible strain relaxation curves were obtained during IHD and only apparent contradictory results, determined by both techniques, were observed.

In fact, high tensile residual stresses were induced by the laser deposit welding operation. However, the final grinding procedure, necessarily applied to produce the fatigue test specimens, induced a very high stress gradient at surface near layers. This strong stress gradient is not detectable by IHD, which can only determine mean stress values in 20 lm minimum depth increments. The use of

XRD enabled the residual stresses at material's surface to be determined, due to its small penetration depth in metallic materials. Therefore, both techniques were satisfactory used as a complement of each other. The high tension values obtained for the residual stresses in the weld deposit, promotes an increase of the effective mean stress, which explain the fatigue results obtained by the authors in a previous work [36].

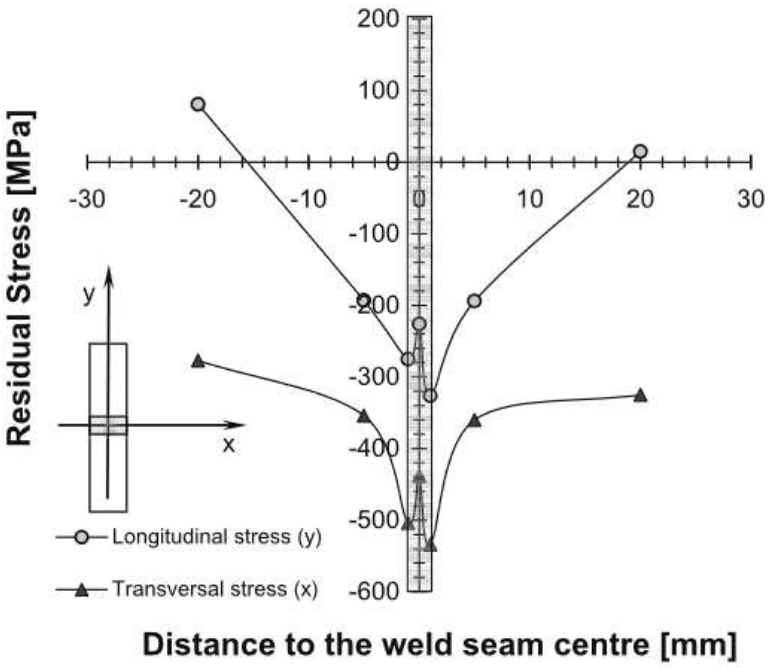

Figure 29: Residual stress distribution at material' surface, in longitudinal and cross directions, of P20 steel specimens [36].

D. Deng and Sh. Kiyoshima [37] studied on Numerical simulation of residual stresses induced by laser beam welding in a SUS316 stainless steel pipe with considering initial residual stress influence. They found the following results: Because the laser beam welding speed is very fast, both the hoop stress distribution and the axial stress distribution along the axial direction of the pipe rarely depend on the central angle around the pipe. Even at the weld start/end, the residual stresses are much close to those on the steady range. At the weld and its vicinity the final residual stresses are not affected by the initial residual stresses and only determined by the welding process. Within the plastic strain range induced by the laser beam welding, the welding process mainly governs the final residual stresses.

However, with the distance from the weld center increases, the influence of the initial residual stresses on the final residual stresses becomes larger. within the range between the critical length (Lhp or Lap) of the plastic strain and the critical length (Lhcr or Lacr) of the residual stress induced by the welding process, the final residual stresses are significantly influenced by the initial residual stresses. In general, when the distance increases the influence of the initial residual stresses on the residual stresses induced by the welding process becomes larger [37].

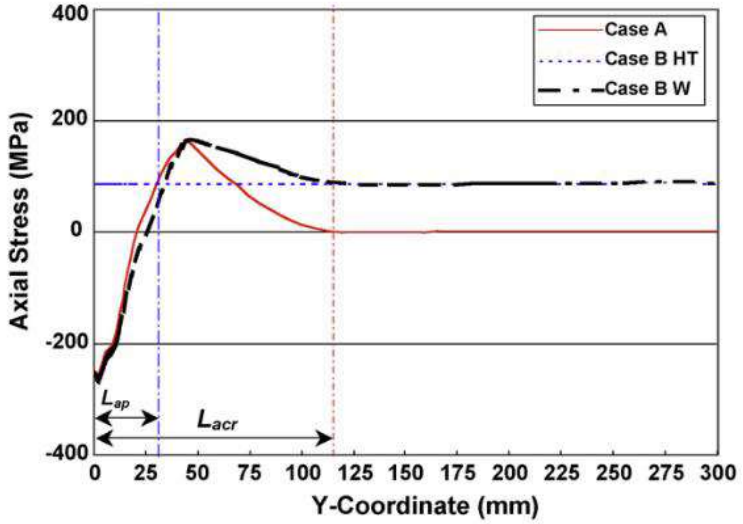

Figure 30: Axial stress distributions on the outside surface with 180◦ central angle [37].

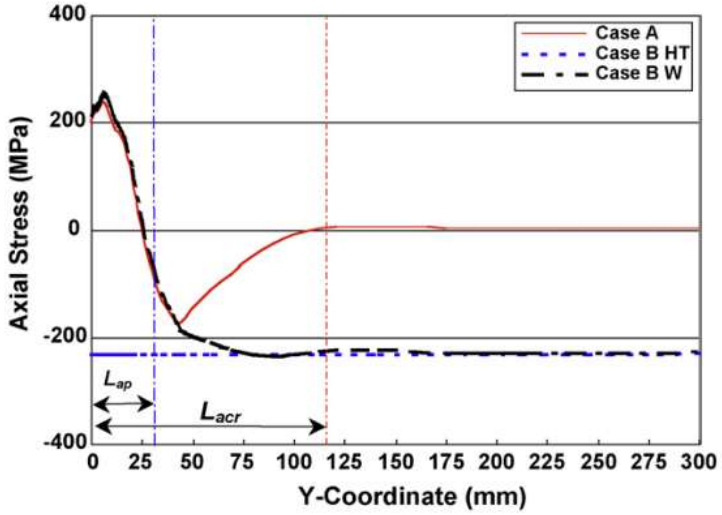

Figure 31: Axial stress distributions on the inside surface with a 180◦ central angle [37].

2-6 Summary of Literature Review and Research Objective:

Based on existing studies, it is evident that laser welding is an effective method for connecting austenitic stainless steel A304, providing suitable joint properties and measuring residual stresses through an appropriate, cost-effective, and accessible method. The measurement of residual stress using X-ray is a non-destructive, economical, and accessible technique. Two major challenges in any welding process are residual stress and distortion. Extensive investigations on these issues have been conducted, particularly in industries such as shipbuilding. Ongoing efforts aim to achieve connections with minimal residual stress and the least amount of distortion, often involving the formulation of a credible standard. In this research, the assessment of residual stress and distortion resulting from laser-welded connections of austenitic stainless steel A304 was measured, an aspect that has not been extensively addressed in previous studies. Such connections find applications in various industries, including pressure vessels and maritime applications. Therefore, achieving these connections with minimal residual stress and distortion is of paramount importance.

Chapter 3: Materials and Research Methodology

3-1 Introduction:

In this chapter, the specifications of raw materials, the welding process, the methodology of conducting tests, and the examination of weld microstructures and associated zones are elucidated. The performed tests encompass tensile mechanical tests, microhardness testing, and residual stress determination using X-ray methods and Distortion. Microscopic examinations also involve the scrutiny of the microstructure of weld areas through optical microscopy. The goal is to evaluate the effect of interlocking welding pattern on metallurgical and mechanical properties of the laser welded joints.

3-2 Material and butt-welded joints analyzed:

In this research, austenitic stainless steel (SS) sheet with the designation 304A ASTM (18-10CrNi5X) was utilized as the base metal. The chemical composition of the parent material is presented in Table 1 while its nominal mechanical properties are reported in Table 2. For elemental analysis and determining the levels of elements present in the base metal and weld metal, the UV Master Foundry Quantum Meter model was employed.

Table 6: composizione chimica percentuale AISI 304.

element	C max	Mn max	P max	S max	Si max	Cr	Ni	Altro
Percentage (%)	0,07	2	0,045	0,015	1	17-20	8-11	N ≤ 0,11

Table 7: Material properties of the parent material.

Property	**Average value**
Young's Modulus	183 GPa
Poisson Ratio	0.27
YTS	333 MPa
UTS	670 MPa

This welding technique uses a laser beam which, focused on the component, transfers energy in the form of heat to the atoms of the material to be welded, allowing various advantages to be obtained. In fact, the melting temperature is reached very quickly, creating a deep, thin, resistant and precise junction because the quantity of molten material is reduced. Furthermore, it is particularly effective on steel and stainless steel because they are metals that absorb laser wavelengths very effectively. The company MAPO S.R.L.S. of Schio (VI) created the two types of welded joints (Figures 32 and 33)

Figure 32 illustrates a view of the prepared specimens for the welding process. The welding parameters are collected in Table 3.

Table 8: laser welding parameters

Welding speed (mm/min)	Spot (mm)	Constraints	Laser power (W)	Focus (mm)	Gas	gas flow rate (l/min)
600	0.27	Table with rulers	600	+3	Nitrogen	20

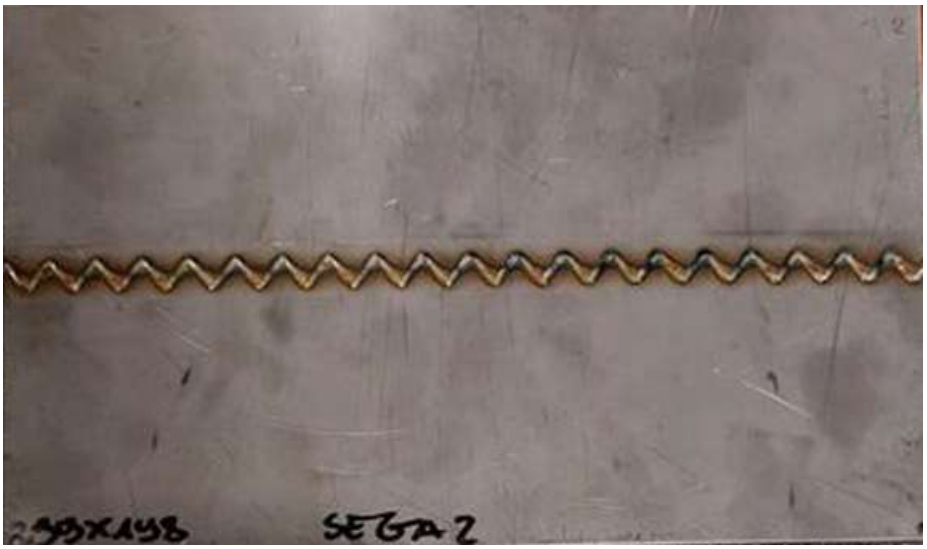

Figure 32: Assembly drawing of sheets with sawtooth weld bead.

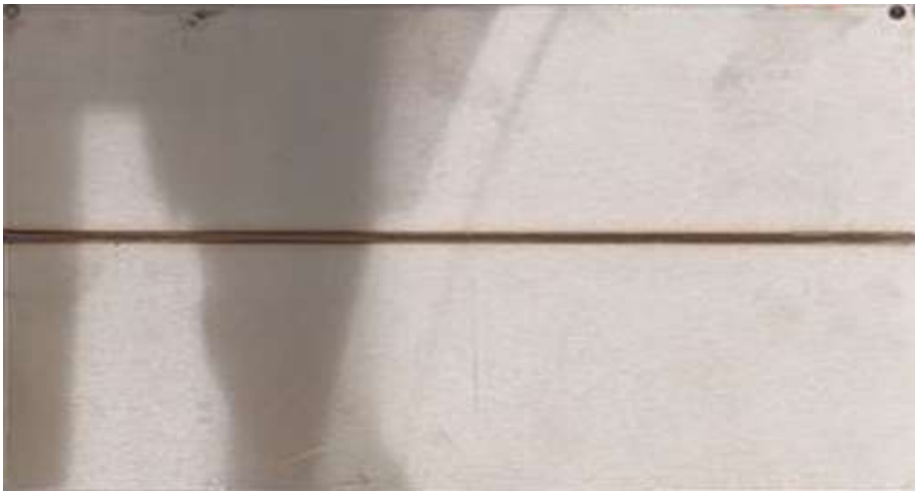

Figure 33: Assembly drawing of sheets with straight weld bead.

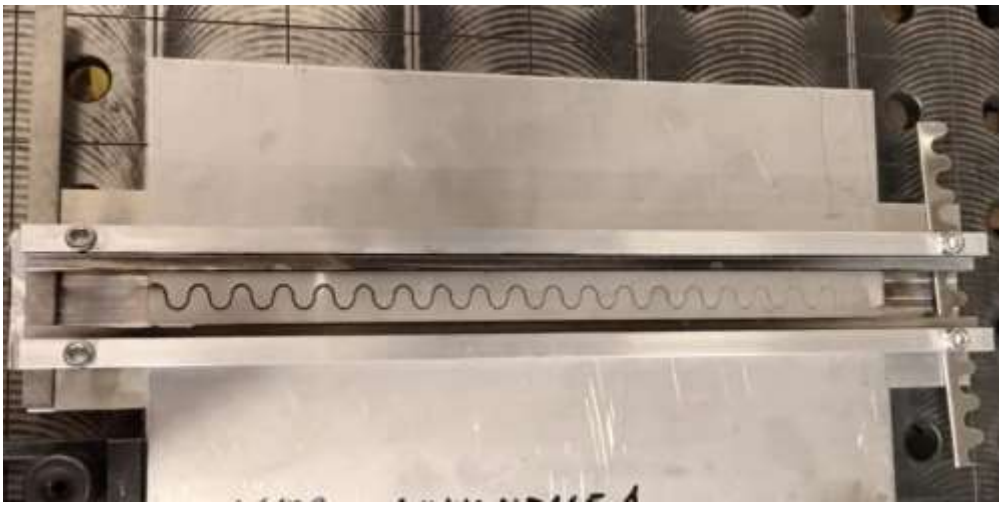

Figure 34: Clamping of the sheet for laser welding (sinusoidal interlocking pattern).

3-3 Microstructural Examinations:

From the welded specimens, cross-sections of the welds were prepared in a manner that encompassed all points, including the base metals, weld metal, and heat-affected zones. The initial and final portions of the weld line, each measuring 25 millimeters, were cut, and specimens for testing were not taken from these areas due to the higher likelihood of defects. After cutting the desired specimens, they were prepared using abrasives ranging from 60 to 3000 grit, and the final polishing was conducted with a water and alumina (Al2O3) mixture using a felt polishing pad. Following the polishing process, a

solution of 4g Cu2SO4, 20 ml HCl, and 20 ml H2O (marble solution) was applied to observe the phases present in different regions of the weld, including the base metal, weld metal, and heat-affected zone, using etching.

3-4 Mechanical Properties

Tests were conducted to determine the mechanical properties of the joint, including X-ray testing for residual stress determination, microhardness testing, tensile testing, and distortion testing.

3-4-1 Microhardness Testing

Microhardness testing was performed using a force of 100 grams at intervals of 500 microns for both base metals, weld metals, heat-affected zones, and joint interfaces. To obtain hardness profiles of the base metals, weld metals, and heat-affected zones, the test was conducted perpendicular to the weld metal. It is worth noting that the application time for this test on the 304A austenitic stainless steel base metal was considered to be 10 seconds.

We initiated the hardness measurements using the FM-810 microhardness tester. Prior to advancing to a higher magnification (500X), it is essential to confirm precise focus at the lower magnification (100X).

Ultimately, we aim to generate a microhardness profile. The interval between hardness measurements is contingent on the size of the weld bead. Given that the Standard width of a weld bead is 0.66 mm, whereas in interlocking it measures 1.44 mm, the measurement step will vary accordingly.

In the end, we will obtain a graph illustrating the variation in hardness concerning distance. Numerous points are measured within the weld bead due to the fluctuating hardness in this region. In contrast, the number of measurements in the base metal (BM) is comparatively lower, indicating that these points are more spaced apart than those measured within the weld bead.

And again, the hardness might change in this area and the closer to base metal lower probability to change the hardness. It is crucial to ensure the perfect alignment of the sample, as any deviation from flatness can yield varying values. The measurement is conducted at the midpoint of the weld bead thickness.

We commence the measurement from one side of the weld bead and proceed to the other, determining the width of the weld bead, which is 0.66 mm for standard welding and 1.44 mm for interlocking welding.

The step for hardness measurement from the center of the weld bead is initially set at 0.1 mm (100 micrometers). When reaching 1 mm, the step changes to 0.5 mm (to the left and right).The applied force during measurement is 100 grams (gf).

3-4-2 Tensile Testing

Tensile strength, yield strength, modulus of elasticity, and ductility (percentage of elongation and percentage of area reduction) were determined. The purpose of the tensile test in this study is to compare the localized strength in welded samples using two welding methods, Standard and Interlocking, and investigate the influence of laser welding on the tensile and mechanical properties of the weld metal. To conduct the tensile test samples were prepared following ASTM E8-00E standards. Three tensile specimens were prepared for each welding condition. The tensile test was performed using a 30-ton Instron model 4486 testing machine from the UK. Figure 35 illustrates the appearance and dimensions of the tensile test specimens. Typically, the specimen length is 15 centimeters, and its width is 1.5 centimeters, and the test is conducted at room temperature. Figure 35 provides a view of the location of the prepared specimens for the tensile test.

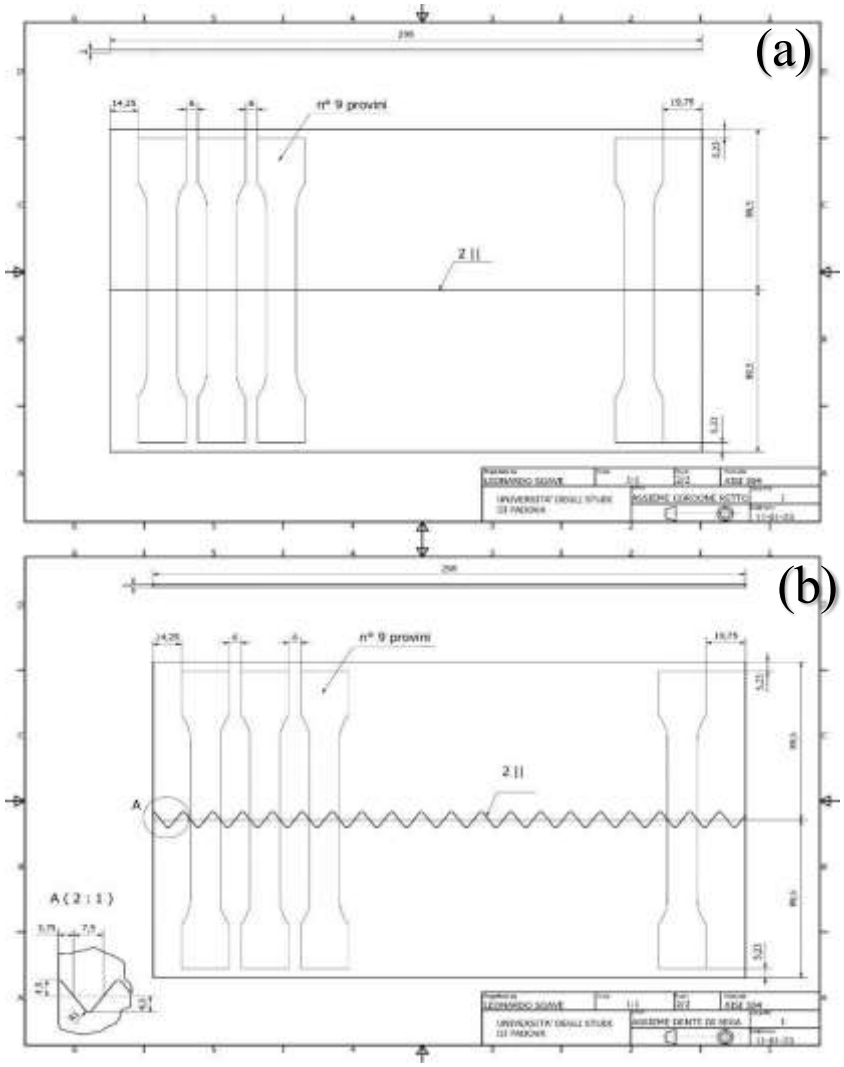

Figure 35: Illustration of the location of the prepared specimens for the tensile test: (a) Standard, (b) Interlocking.

3-4-3 Residual Stress Examination

This test is conducted to determine and evaluate residual stress along the length of the weld. Figure 35 presents the components of residual stress and the measurement paths for residual stress. Table 3-2 provides the parameters for measuring residual stress using the X-ray diffraction method, along with the adopted device specifications and experimental parameters.

We conducted scans in both directions—parallel and perpendicular to the weld line. Initially, we initiated scanning in the transverse direction. In general, parallel and perpendicular stresses differ due to variations in cooling and heat flow, resulting in asymmetric distortion. It is hypothesized that parallel stresses may be higher, potentially influenced by preheating conditions.

According to the Bragg formula, 2θ represents the diffraction angle (the angle between the incident and diffracted arrays), and D signifies the distance between layers of atoms. Our focus is not on the entire diffraction pattern but on a fixed plane—specifically, the (311) plane at 42 degrees for austenitic steels. By doing so, we identify peaks corresponding to particular crystallographic directions, adhering to the Bragg law. When stress is applied, the distance between lattice layers changes. By measuring the resulting shift, we can quantify the amount of residual stress. Additionally, the broadening and narrowing of peaks indicate changes in grain size, a parameter not directly measurable through XRD. Notably, while the angle between the source and detector remains constant, the angle (ψ) between the emitting array and the specimen changes.

In the case of austenitic steel, particularly stainless steel, we focus on the (311) peak using a chromium source. It's important to note that a copper source is incapable of measuring this specific peak.

When we focus on the (311) peak, the software identifies it without accounting for the residual stress. The key aspect of residual stress measurement lies in the data trend. Therefore, we measure eleven different angles from -30 to +30 degrees. The analysis involves examining trends in the negative and positive parts of the spectrum. If both trends are increasing, it indicates tensile stress, while a decrease in both signifies compressive stress.

Using this technique, we observe how a specific peak shifts. The scan is conducted at various angles (ψ).

The measurement process involves the following steps:

1. Set up the apparatus in the proper position.
2. Increment the Psi angle (in this case, at 11 different angles). At each angle, a peak is acquired.
3. Gather a series of measurements from various angles, and through the use of software, fit these points (centroids). This fitting process provides the precise value of stress.

The Psi angle is determined by the goniometer, while 2θ is the fixed angle between the detector and source. The variable we manipulate in this process is the Psi angle.

We opted for a 0.5 mm collimator size for the laser, but it's worth noting that the spot size may exceed 2 mm. To confirm this, we can use fluorescent paper. This collimator size is the smallest available. The X-ray source is chromium, and a vanadium filter is used. Adjustment of the height is necessary to ensure that the spot being measured is at the center of the goniometer. The range of Psi angles being measured spans from -30 to +30 (with the maximum measurable angle limited to between -45 to +45) due to the geometry of our plates, preventing any collision with the detector.

If we envision the goniometer's movement path as the radius of a circle, the angle ranges from -30 to +30. Due to the size of our plates, there's a risk of hitting the detector. The software we utilize is stress.net. Initially, we set the time to 30 seconds, but the intensity was insufficient. To enhance the signal, we increased the time to 180 seconds, aiming for higher peaks with 11 positions per point. This adjustment resulted in 33 minutes for each point. For each material and condition, it was crucial to determine the optimal settings for a satisfactory measurement, considering both time and the number of positions. Subsequently, due to unsatisfactory signal strength, we extended the time to 300 seconds with 11 positions per point.

Initially, before commencing the process, we adjust the height in the Z direction. Subsequently, the machine attempts to find the correct position to adhere to the Bragg law. We begin with a single point to ensure that the time and intensity are correct. The machine then provides us with a stress value (not physical parameters) for that specific point.

So:

- Define the positions of the peaks.
- Measure the amount of shift.
- Determine the lattice spacing (d).
- Measure the strain (e) by knowing the lattice spacing (d).
- Consider the Young's Modulus (E) as 205 GPa and Poisson's Ratio (ν) (according to the professor's suggestion).

For each position (the 11 measured angles), we have a corresponding lattice spacing (d). We use something akin to an average as a representative value of the real d spacing. The objective is to comprehend how the peak is shifting and express it as a function of d to derive the stress (σ). This method involves fitting d as a function (Fig. 35).

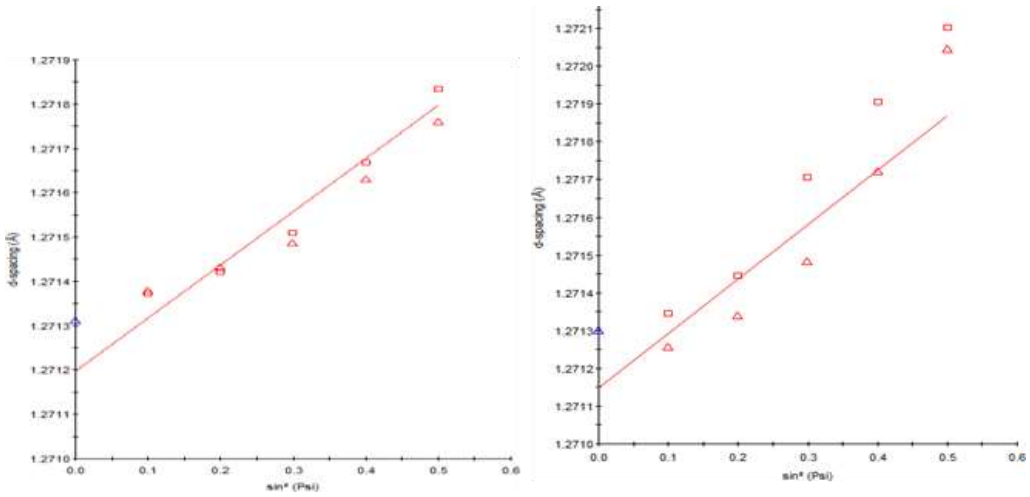

Figure 35: example of data fitting.

As an example, we obtained a stress value of 445 MPa with a confidence level of 98%, which is considered good. We can generate various graphs, such as one depicting spacing versus Psi angle (representing the change in interlunar spacing) and another illustrating the shift of the peak compared to Psi angle (indicating how these peaks move in comparison to a stress-free position).

For example, in the ideal condition of 304 steel, in the absence of stress and strain, our metal sheet exhibits a certain pattern without any welding. In this scenario, 2θ is constant, and we vary the Psi angle. By observing how this peak moves in comparison to the well-known original position, we can infer the shift caused by tensile or compressive stress. We measure various shifts and analyze them accordingly.

3-4-5 The process that the software follows is automated.

Based on the Psi angle, we measure the shift of the peaks, resulting in a variation in the d spacing. This implies a certain strain, and by using Poisson's ratio and Young's modulus (the elastic constant of the material), we can calculate the stress (σ). We simply need to specify a function or method (such as centroid) to fit all the d values and obtain the average d for use in this formula.

In the centroid method, you identify the peak, determine the background, locate the center of the peak, and ascertain its height. This method is based on fitting the peak. The purpose of the last point on the sheet is to compare the residual stress before welding, which may include stresses from hot rolling, cold rolling, milling, or cutting. Points where residual stresses are assessed are schematically shown in Figure 36.

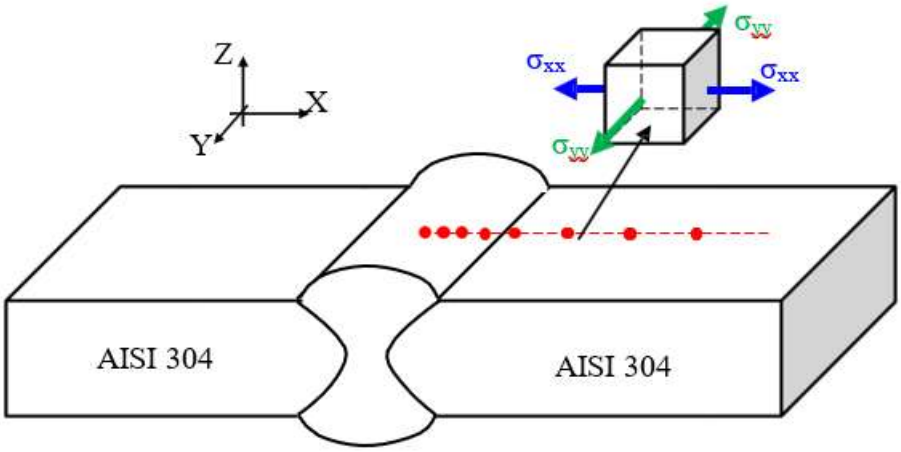

Figure 36: Residual stress components and paths for residual stress measurement.

Table 9: Residual stress measurement by the X-ray diffraction method: adopted device and experimental parameters.

Surface preparation	-
X-ray device	GNR Spider X
Radiation	Cr-Kα with Vanadium filter, penetration depth 15 μm
Collimator size	0.5 mm
Method	*Centroid*
Measurement paths	see Fig. 1
Residual stress components	σ_{XX} and σ_{YY} (see Fig. 3-6)
Acquisition time	300 s/ψ angle
ψ − angles	11 ψ-angles -30° < ψ < 30°
Elastic constants	E = 220 GPa, ν = 0.34

3-5 Distortion Examination

Coordinate Measurement Machine (CMM Hybrid) was used with both optical and tactile probe systems to comprehensively measure the deformation of two samples in both standard and interlocking configurations. For precision, we gather data at a rate of 1 point per millimeter. As a result, each line along the length comprises 251 points, and each line across the width contains 131 points. Measurements are taken in both longitudinal and transverse directions to enhance measurement accuracy by a few millimeters.

Subsequently, the collected data undergoes processing in MATLAB software to generate images. In these images, the color red represents maximum values, while blue indicates minimum values, regardless of a specific criterion being measured. The probe's movement speed is approximately 5 millimeters per second, ensuring efficient data collection for a comprehensive analysis of changes.

Chapter 4: Results and discussion

4-1 Introduction

Figure 4-1 illustrates the surface appearance of the welded samples. Figure 37-a corresponds to a Standard welded sample, while Figure 37-b corresponds to an Interlocking welded sample whose geometrical parameters of the welding pattern were described in the previous chapter.

As observed in Figure 37, the width of the weld in the Standard configuration is much less than in the zigzag configuration. This results in an increase in the heat-affected zone despite the welding speed was kept constant.

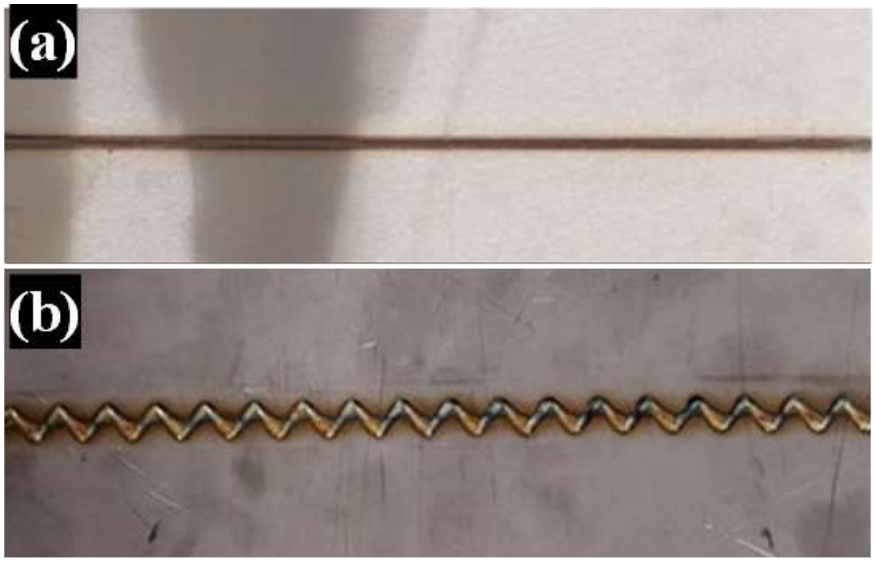

Figure 37: Welded plates, where (a) represents a Standard (linear) configuration, and (b) represents an interlocking (zigzag) configuration.

4-2 Macrostructure

Figure 38 provides a cross-sectional view of the weld macrostructure for the welded samples. In this image, Figure 38-a, corresponds to a Standard welded sample, and Figure 38-b corresponds to a zigzag welded sample. As observed in Figure 38, the width of the weld in the Standard configuration is less than that in the interlocking configuration. This can be attributed to the accumulation of the heat due to the sinus pattern, resulting in an increase in heat input to the weld.

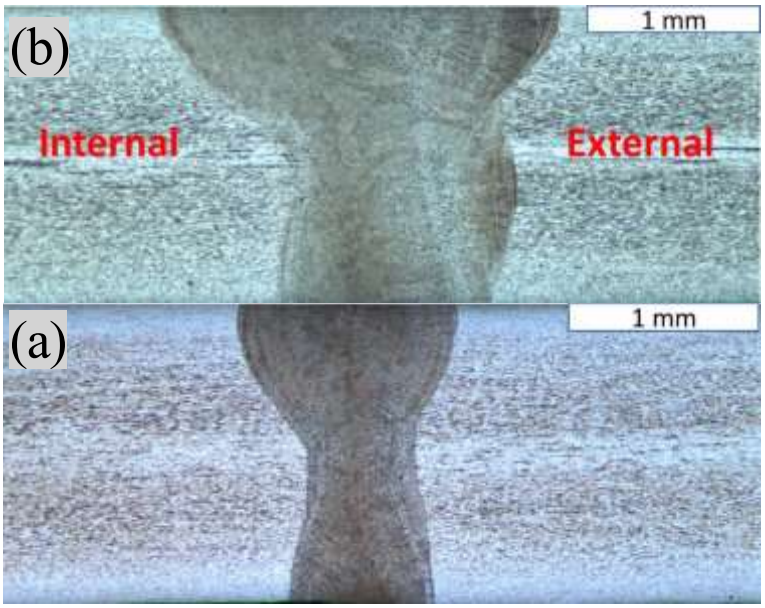

Figure 38: Macrograph of the weld cross section: (a) Standard (linear), (b) Interlocking.

4-3 Microstructure

Figure 39 shows the microstructure of the base metal of austenitic stainless steel 304A. As observed, the microstructure of the base metal of austenitic stainless steel 304A exhibits a wrought structure consisting of an austenitic matrix along with delta ferrite. In these images, the austenitic matrix is highlighted in a bright color, while the delta ferrite phase is visible in a darker color. The delta ferrite is elongated in a strip-like manner in the rolling direction, and its formation is a result of the segregation of ferrite-forming elements (especially chromium) during solidification.

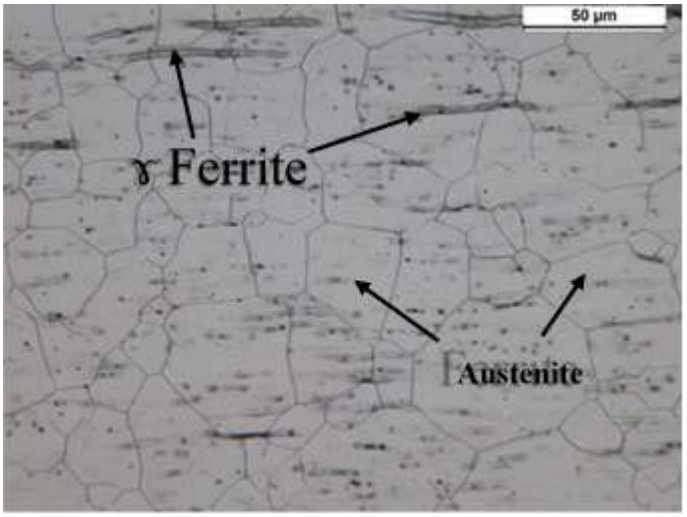

Figure 39: Microstructure of A304 stainless steel base metal.

Figure 40 illustrates the microstructure of different regions in a Standard welded sample, including the heat-affected zone and the weld metal. Figure 40-a, depicts the microstructure of the heat-affected zone in the Standard welded sample.

In austenitic stainless steels, due to their low thermal conductivity, the width of the heat-affected zone is very small. As seen in Figure 40-a, a noticeable phenomenon in the heat-affected zone of this steel is the increased presence of delta ferrite bands. The formation of delta ferrite is attributed to the slow transformation of austenite to ferrite and the rapid nature of the heat cycle in the heat-affected zone. The level of delta ferrite formation is relatively low due to the sluggish transformation of austenite to ferrite and the rapid thermal cycle in the heat-affected zone.

The limited formation of delta ferrite is due to the slow transformation of austenite to ferrite and the rapid thermal cycle in the heat-affected zone. In this region, the morphology of the delta ferrite, which has solidified in a skeletal structure, is clearly visible. Additionally, as the progression goes from the base metal towards the weld metal in the heat-affected zone, the austenite grains transition from a rounded and co-axial shape to an increase in grain size. This phenomenon occurs because the heat input is higher in areas close to the weld metal, leading to the re-crystallization and coarsening of austenite grains in this region.

As observed in Figure 40-a, in the heat-affected zone, the formed ferrites along the grain boundaries exhibit a co-axial growth pattern. This is attributed to the moderate cooling rate of the weld and the low Nieq/Creq ratio. The ferrites formed along the grain boundaries restrict the grain growth, reducing the likelihood of cracking in the fusion zone of the HAZ.

In other words, the ferrites formed in the common fusion zone of the weld metal and the austenitic base metal extend along the existing ferrites in the austenitic matrix of the base metal. Initially, austenite grows epitaxial from the un-melted austenite grains at the fusion boundary, and then delta ferrite nucleates at the forefront of the solidification. This type of growth is beneficial for welding because it ties the weld zone to the base metal grains, preventing stress concentration in the fusion zone and HAZ.

Figure 40-b depicts the microstructure of the weld metal in the heat-affected zone of the Standard welded sample. As evident in Figure 40-b, the microstructure in this region appears as a skeletal ferrite and, in some areas, as ferrite networks accompanied by austenite.

The morphology of the skeletal or worm-like ferrite structure occurs when the cooling rate is moderate or when the Nieq/Creq ratio is within the ferrite-austenite (FA) range. This results in the development of austenite consuming the ferrite until the ferrite becomes sufficiently enriched in ferrite-forming elements (chromium and molybdenum) and depleted in austenite-forming elements (nickel, carbon, and nitrogen) and stabilizes at lower temperatures where the diffusion rate is limited.

In some areas, the ferrite structure appears as networks. The network morphology arises due to constrained diffusion during the ferrite-austenite transformation, resulting in a network structure instead of a skeletal one. As the diffusion distances decrease, the transformation process is facilitated, leading to the formation of more compact network structures.

This results in the formation of a remaining ferrite pattern that has interrupted the growth direction of the primary cell or dendrite. Therefore, the structure created on the weld surface, due to the high cooling rate and a higher Nieq/Creq ratio, appears in the form of networks.

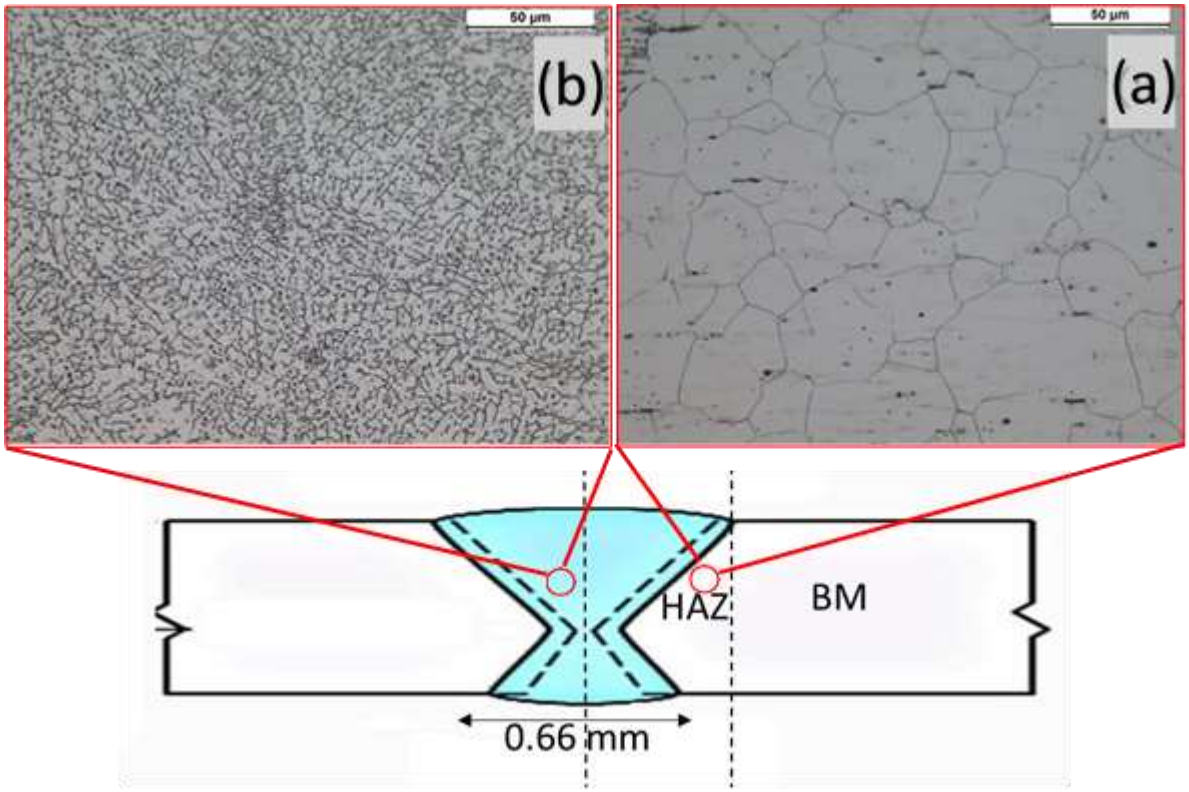

Figure 40: presents the microstructure of different regions in the Standard welded sample, including the heat-affected zone and the weld metal.

As seen in Figure 41, there is no observable change in the microstructure of different regions between the samples welded using the interlocking method and the one welded using the Standard method.

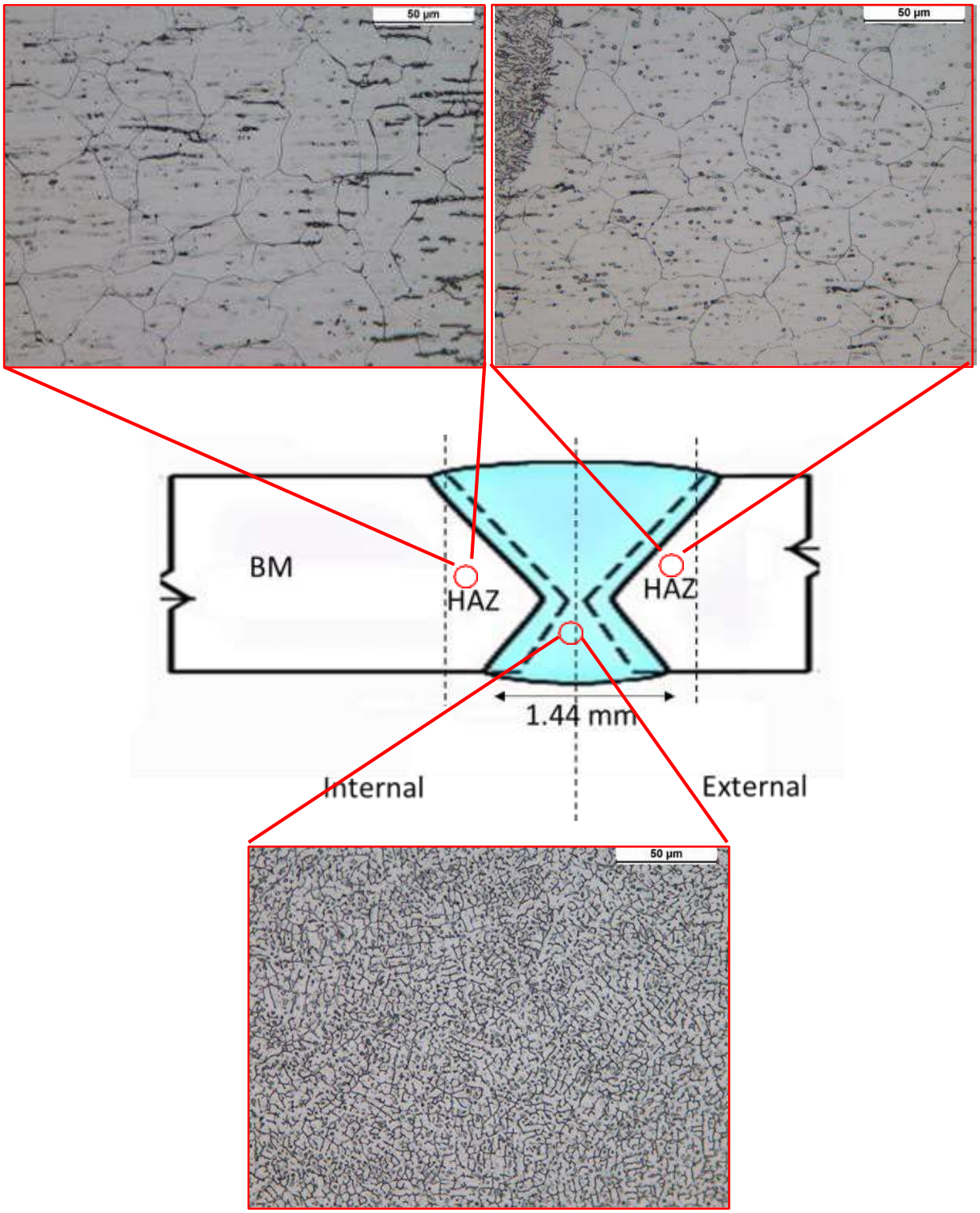

Figure 41: Microstructure of sample (Interlocking).

4-3 Grain size

Figure 42 provides a comprehensive view of the measured grain size areas from the cross-sectional surface of the Standard welded sample. Table 1-4 presents the grain sizes measured in the designated areas shown in Figure 42. As observed, grain sizes have been measured at four points in the heat-affected zone, with an average grain size of approximately 7.5 micrometers in this area. Additionally, grain sizes have been measured at four points in the base metal area, with an average grain size of about 7.625 micrometers in the base metal region. It is evident that there is a negligible change in grain size, with a reduction of approximately 1.614% in the heat-affected zone, which is very small and can be overlooked.

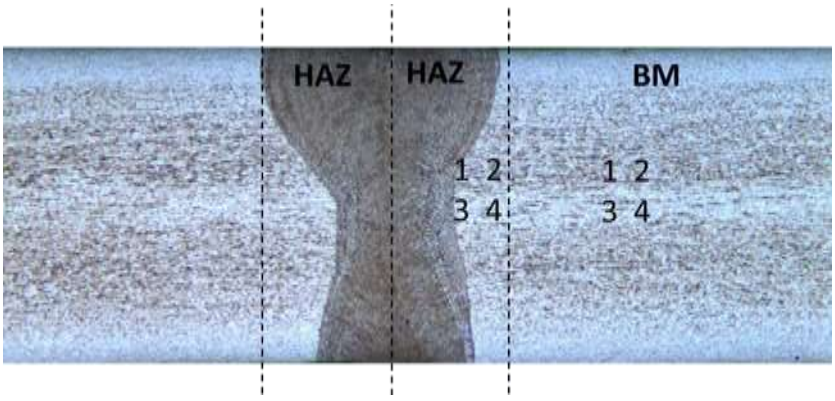

Figure 42: Grain Size Measurement Areas.

Table 10: Grain Size of the designated areas in Figure 42.

	Zone No.	Grain size	Grain size Av.
HAZ	1	7.5 ± 0.1	7.5 ± 0.1
	2	7.5 ± 0.1	
	3	7.5 ± 0.1	
	4	7.5 ± 0.1	
BM	1	7.5 ± 0.1	7.625 ± 0.1
	2	7.5 ± 0.1	
	3	8 ± 0.1	
	4	7.5 ± 0.1	

Figure 43 provides a general view of the measured grain size areas from the cross-sectional surface of the sample welded using the Interlocking method. Table 4-2 displays the grain sizes measured in the designated areas shown in Figure 43. As seen in Figure 43, grain sizes have been measured at four points in the heat-affected zone, with an average grain size of approximately 8.125 micrometers in this area. Additionally, grain sizes have been measured at two points in the base metal area, with an average grain size of about 7.5 micrometers in the base metal region. It is noticeable that there is a negligible change in grain size, with a reduction of approximately 8.5 % in the base metal zone.

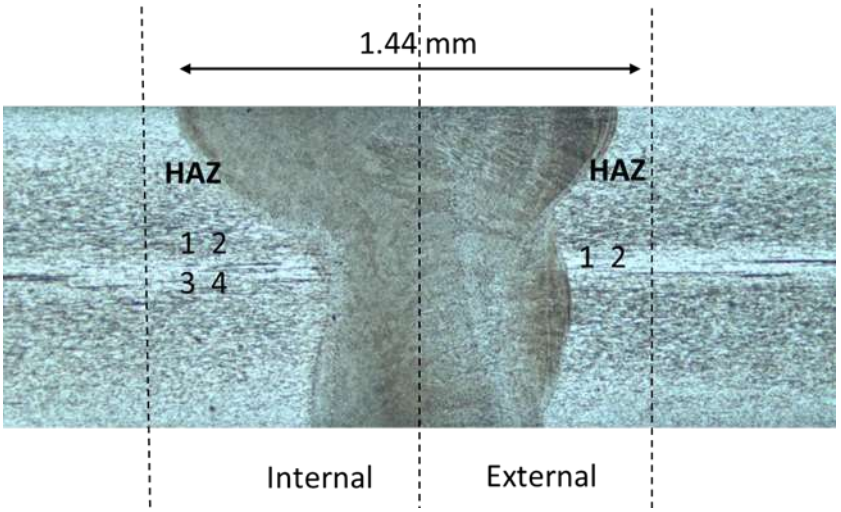

Figure 43: Grain Size Measurement Areas

Table 11: Grain Size of the designated areas in Figure 46 (ADD standard deviations)

	Zone No.	Grain size	Grain size Av.
Internal HAZ	1	8.5 ± 0.1	8.125 ± 0.1
	2	8 ± 0.1	
	3	8 ± 0.1	
	4	8 ± 0.1	
External BM	1	7.5 ± 0.1	7.5 ± 0.1
	2	7.5 ± 0.1	

Considering the obtained results, it is observed that the grain size in the sample welded Standard is approximately 7.625 micrometers, while in the sample welded using the interlocking method, it is around 8.125 micrometers. Given that the heat input (P/v) was kept constant during welding, the effect of interlocking pattern resulted in a sightly increase of grain size in HAZ due to the less efficient heat dissipation which the interlocking pattern is associated to.

4-4 Microhardness

Images 44 and 45 respectively depict profiles of hardness for welded samples using the Standard and Interlocking methods, along with the microstructure of different regions subjected to hardness testing. The horizontal hardness results presented in Figure 44 indicate a generally mild ascending trend from the base metal towards the weld metal. As shown in Figure 44, it is observed that the hardness of the base metal of the austenitic stainless steel is within the range of 180 Vickers. In the heat-affected regions, a noticeable increase in hardness is observed compared to the base metals, reaching approximately 220 Vickers at the center of the weld metal.

The increase in hardness is observed in the heat-affected zone compared to the base metal. Considering that ferrite is a phase harder than austenite, this increase in hardness can be attributed to the higher presence of ferrite phase in this zone compared to the base metal. The reason for this is that during welding, more heat is introduced to this area compared to the base metal. Furthermore, it is evident that the microhardness in the weld metal is higher than in the base metal and the heat-affected zone.

Figure 45 presents a comparative chart of the microhardness of welded samples using both methods. As observed in Figure 45, the microhardness in the weld metal region in the Interlocking configuration is approximately 30 Vickers less than the sample welded in the Standard configuration. Since the ferrite phase is harder than the austenite phase, this increase in hardness can be attributed to the higher amount of ferrite in the weld metal of the sample welded in the Standard method compared to the weld metal of the sample welded in the interlocking method.

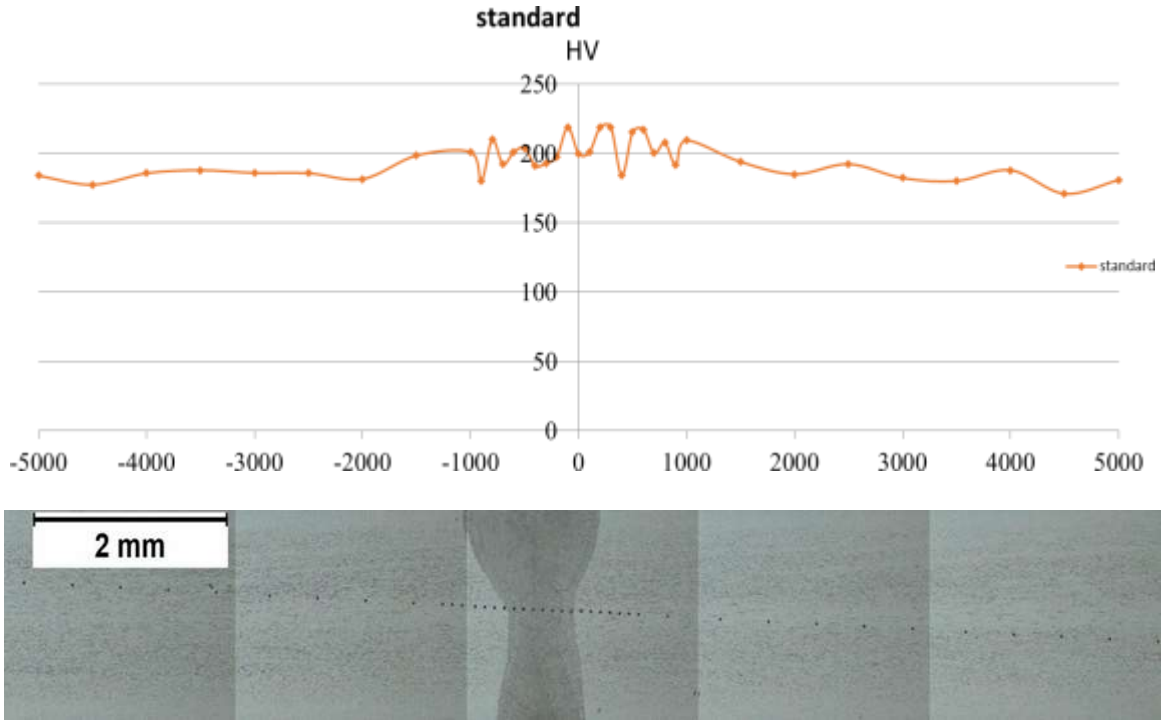

Figure 44: The Microhardness profile of standard sample.

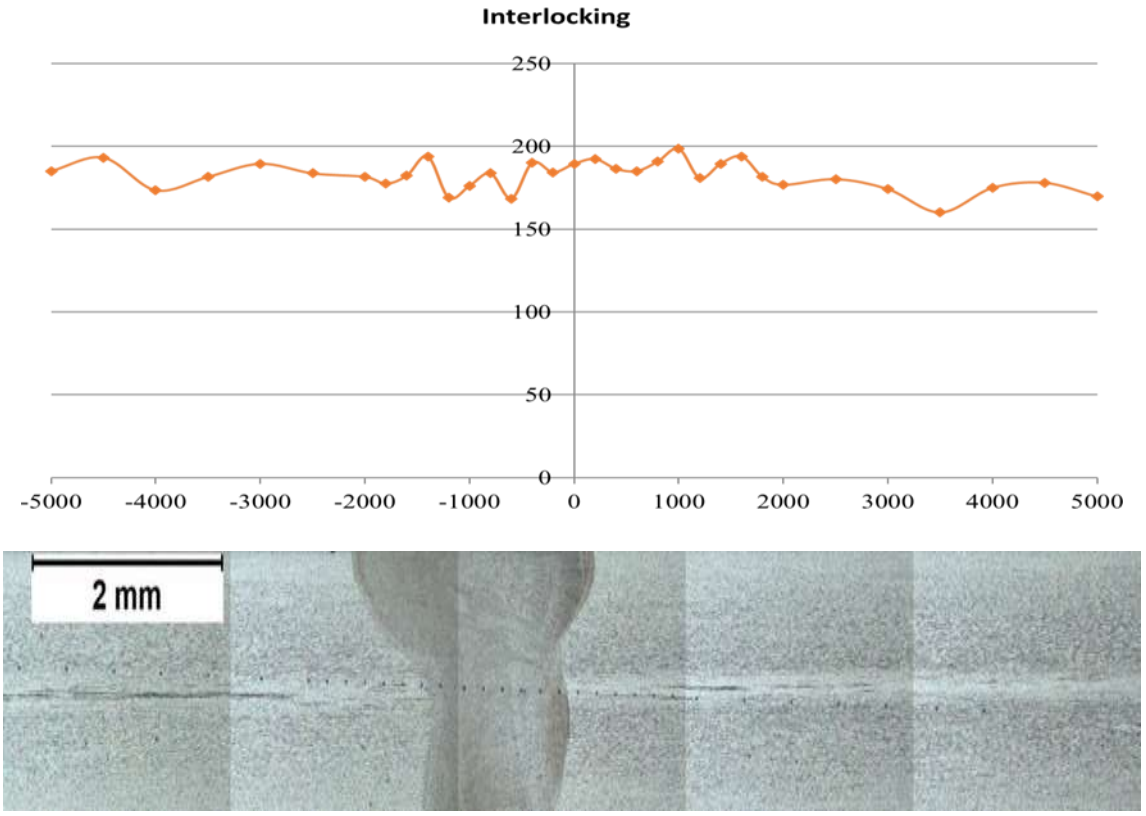

Figure 45: The Microhardness profile of interlocking sample.

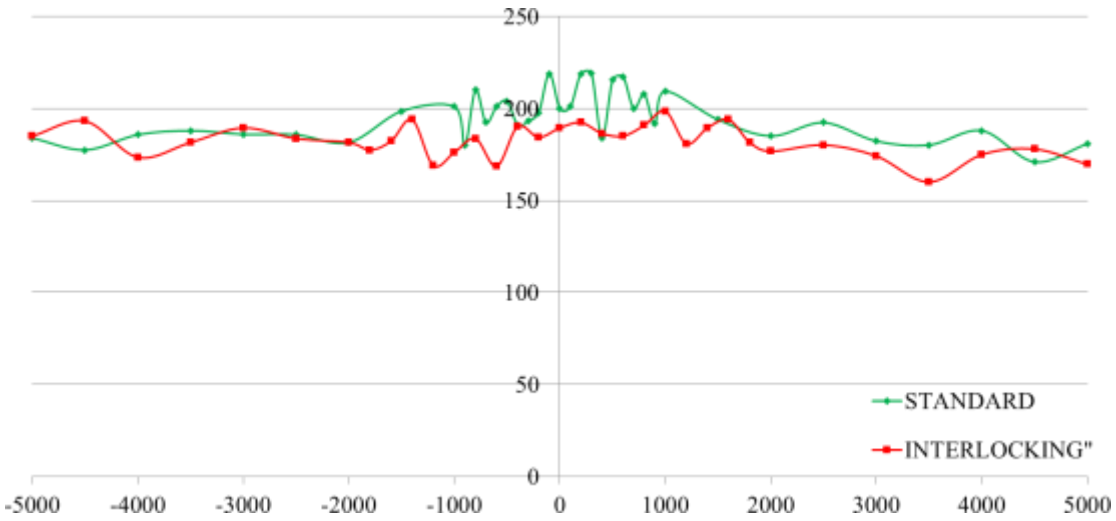

Figure 46: is a comparative chart of the microhardness of welded samples.

4-5 Tensile Test

In Table 46, the tensile test results for the welded samples are provided. According to the obtained results in the tensile test, it is observed that the ultimate tensile strength and yield strength for the sample welded using the Standard method are 671 and 294 MPa, respectively. Additionally, the ultimate tensile strength and yield strength for the sample welded using the Interlocking method are 679 and 317 MPa, respectively.

Table 12: presents the results of the tensile test for the welded samples.

Specimen	YS (MPa)	UTS (MPa)	Elongation (%)
Standard	274	671	51
Interlocking	317	679	52

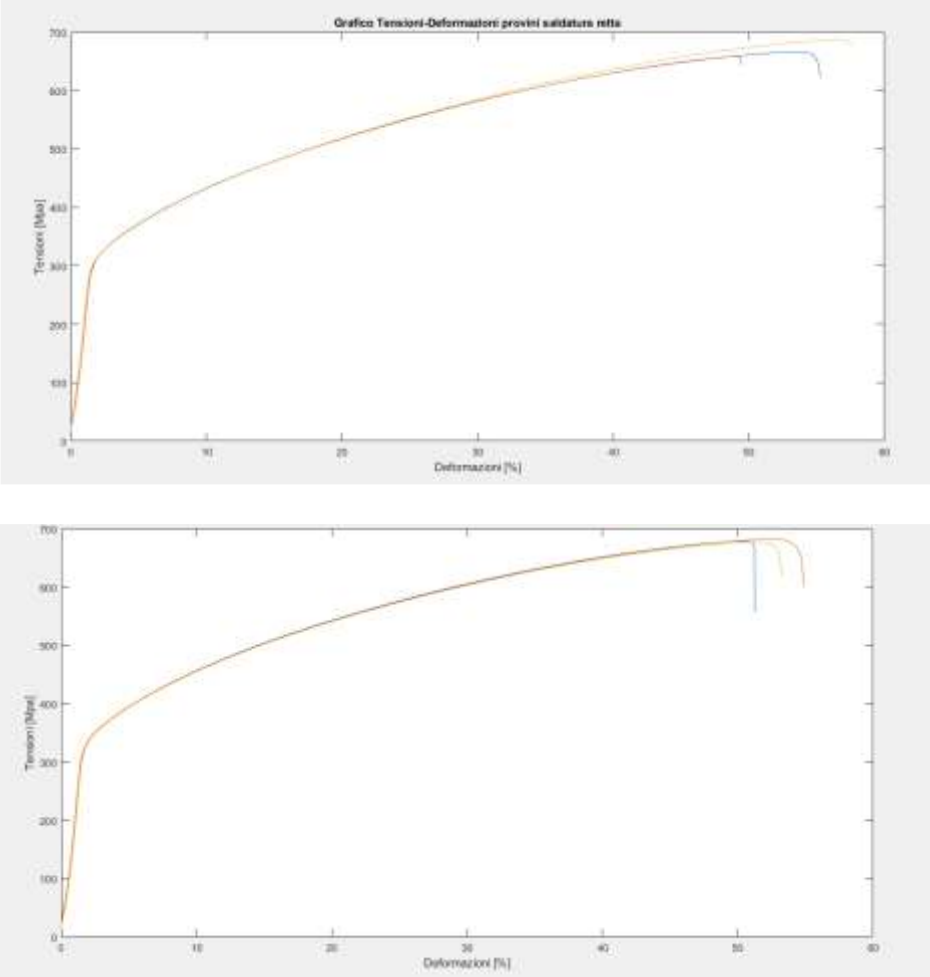

Figure 46: Strain Stress Graph of (a) Straight Weld Specimens (b) sinusoidal weld specimens

4-6 Residual stress

Figure 47 provides an illustration of the location where the X-ray diffraction test was conducted to measure residual stress. Additionally, in Figure 48, a plot of transverse and longitudinal residual stress is presented. As seen in Figure 48, the residual stress is in the form of tensile residual stress in both transverse and longitudinal directions.

Figure 49 presents an illustration of the location where the X-ray diffraction test was conducted to measure residual stress. Additionally, in Figure 49, a plot of transverse and longitudinal residual stress is provided. As seen in Figure 49, the residual stress appears in both tensile and compressive forms in the transverse and longitudinal directions. It is evident, as shown in Figure 49, that in standard welding and in transverse residual stress in the heat-affected zone, the stress is compressive.

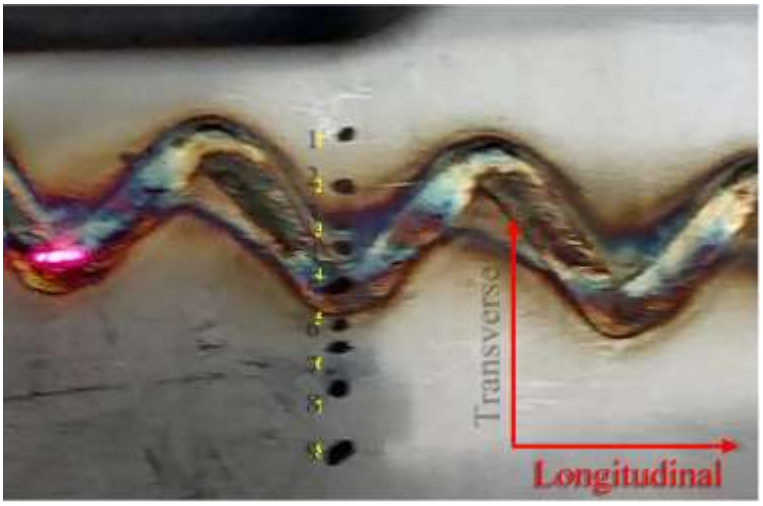

Figure 47: is an illustration of the location where the X-ray diffraction test was conducted to measure residual stress.

During the welding process, the solid metal (weld metal) replacing the molten metal occupies less space, meaning that the density of the solid metal is higher. The molten metal also contracts, causing the surface of the weld pool to decrease below its initial level. However, simultaneously, the subsequent molten metal resulting from the melting of the base metal feeds this region at the front of the molten pool. Therefore, although significant contraction occurs during cooling and the transition from the molten to solid state, the weld surface usually does not exhibit it unless the amount of filler material is insufficient to compensate for the volume reduction.

If there are no obstacles, each of the sheets on either side of the weld line tends to bend due to the pressure resulting from the contraction of the weld line. However, in practice, such a curved weld seam does not form. Therefore, it can be concluded that compressive residual stresses occur in the areas between the weld metal and the base metal (heat-affected zone), and tensile residual stresses occur in the central regions of the weld line.

Residual stress is primarily a result of compressive yielding that occurs around the molten region due to heating and material expansion during welding. When the weld metal cools, it contracts, leading to the development of tensile residual stress, especially in the longitudinal direction. After welding, tensile residual stress remains along the weld centerline, causing the generation of compensating compressive stress, particularly in the weld region.

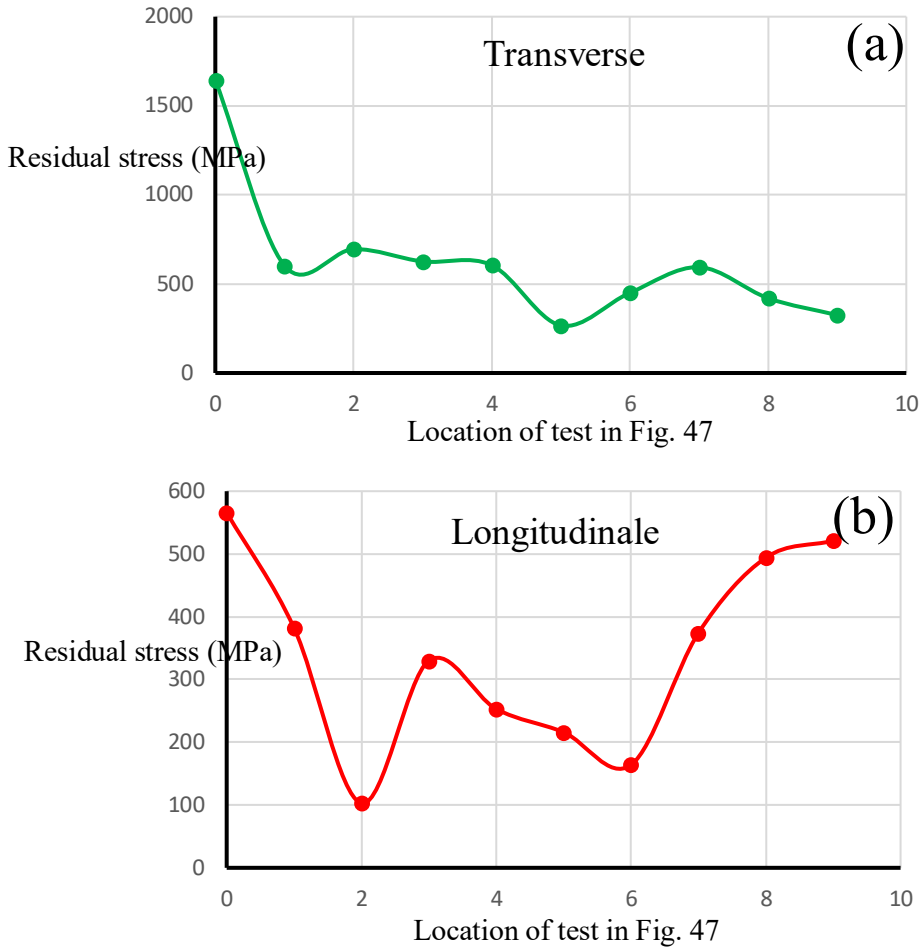

Figure 48: Residual stress diagram (a) transverse (and) longitudinal.

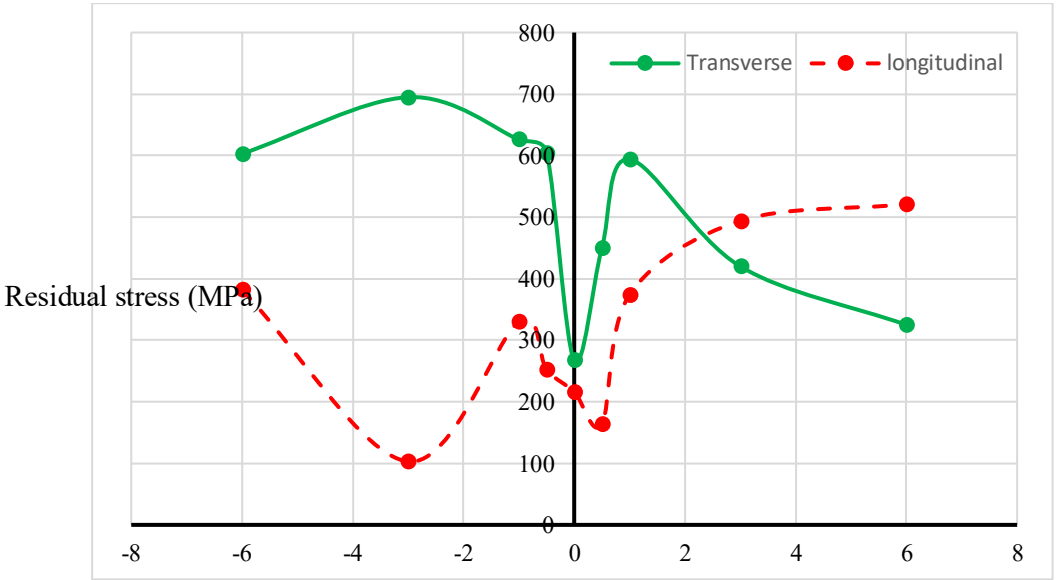

Figure 49: transverse and longitudinal residual stress diagram.

Table 13: Numerical results of longitudinal and transverse residual stress testing at various points

point	distance(mm)	RS (MPa) (transverse)	error	RS (MPa) (longitudinal)	error
-	Far away from weld	1645	±17	566	±21
1	-6	603	±13	382	±20
2	-3	695	±14	103	±17
3	-1	626	±14	330	±20
4	(edge of weld)-0.5	605	±15	253	±19
5	0	267	±21	216	±24
6	(edge of weld) 0.5	450	±14	164	±26
7	1	594	±16	374	±24
8	3	420	±16	494	±24
9	6	325	±18	521	±21

The indentation in the profiles of longitudinal residual stress at the weld center can be attributed to strains associated with ferritic and austenitic transformations, including volumetric expansion during the cooling of the welding regions, encompassing the entire Fusion Zone (FZ) and the majority of the Heat-Affected Zone (HAZ). Additionally, it can be demonstrated that the strains related to ferritic and austenitic transformations can compensate for thermal contraction in the FZ and HAZ, particularly for ferrite.

Austenitic stainless steels, which can typically reverse or at least mitigate tensile stresses within the FZ, play a role in this compensation. The M-shaped profiles contrast with profiles of non-transforming materials, where a single tensile peak is expected at the weld center or near it, diminishing into low surface compressive stresses in the surrounding field.

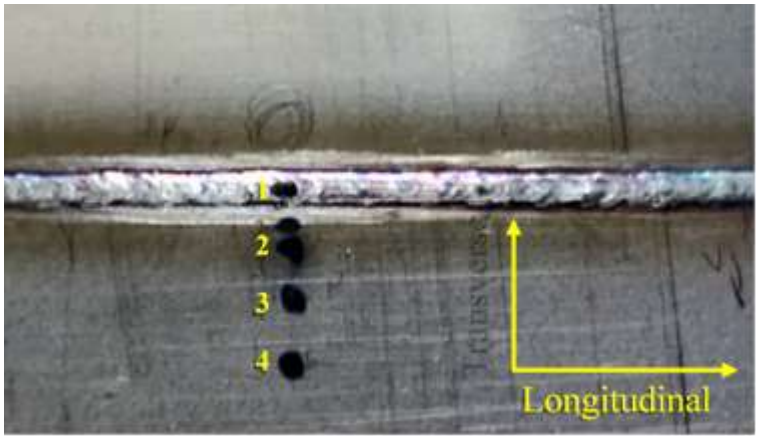

Figure 50: illustrates the location where the X-ray diffraction test was conducted to measure residual stress.

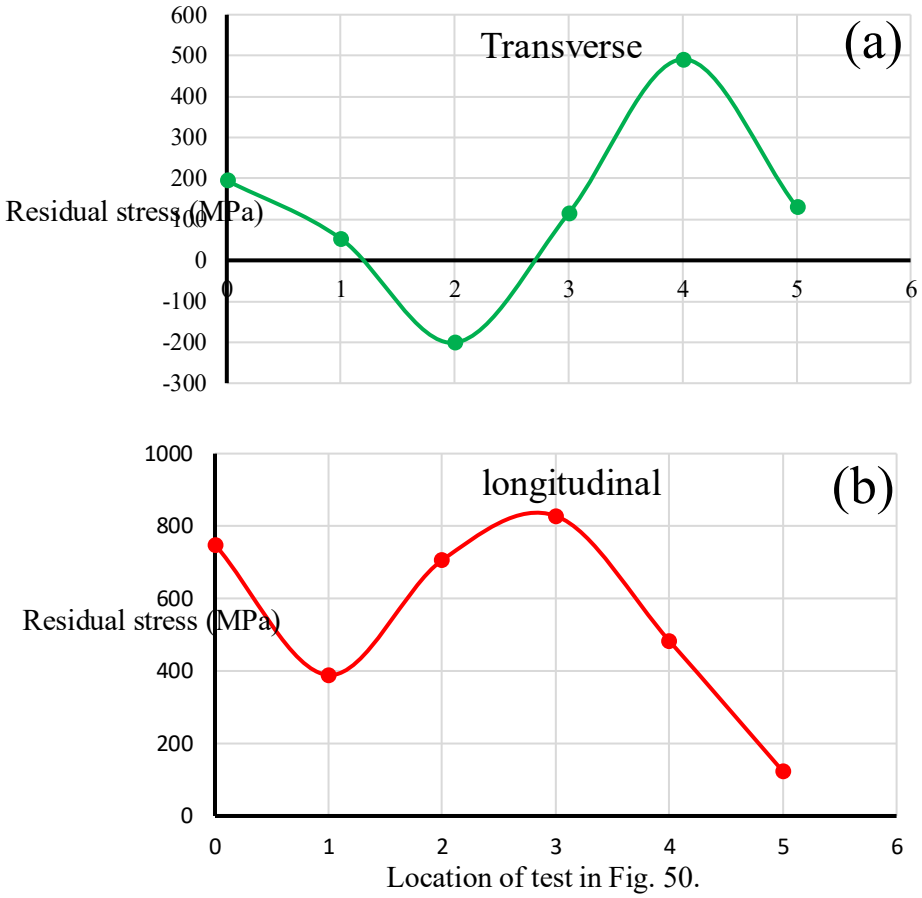

Figure 51: Residual stress diagram (a) transverse (and) longitudinal.

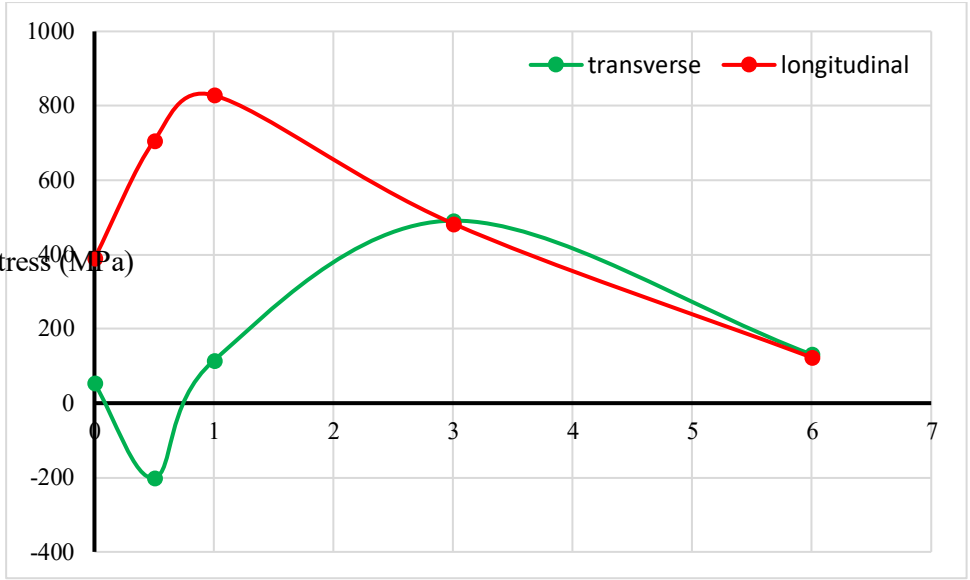

Figure 52: transverse and longitudinal residual stress diagram.

4-7 Distortion

Figure 53 illustrates the distortion angle diagram of the Standard welded sample. As seen in Figures 53 and 54 for the Standard welded sample, changes in the angle of distortion at points 0, +10, +20, +30, +40, +50, and +60 are 2.047, 2.045, 2.033, 2.035, 2.043, and 2.058 degrees, respectively. It is also observed that changes in the angle of distortion at points 0, -10, -20, -30, -40, -50, and -60 are 2.047, 2.148, 2.187, 2.228, 2.268, and 2.305 degrees, respectively. The results indicate that as one moves away from the center, the changes in the angle of distortion increase. According to the obtained results, it can be observed that the changes in the angle in the Standard welding state are almost 12.6% relative to the centerline.

The changes in the height of distortion at points 0, +10, +20, +30, +40, +50, and +60 are 1.312 1.198, 1.207, 1.219, 1.231, and 1.270 degrees, respectively. Additionally, it is observed that the changes in the height of distortion at points 0, -10, -20, -30, -40, -50, and -60 are 1.321, 1.270, 1.298, 1.327, 1.355, and 1.380 degrees, respectively.

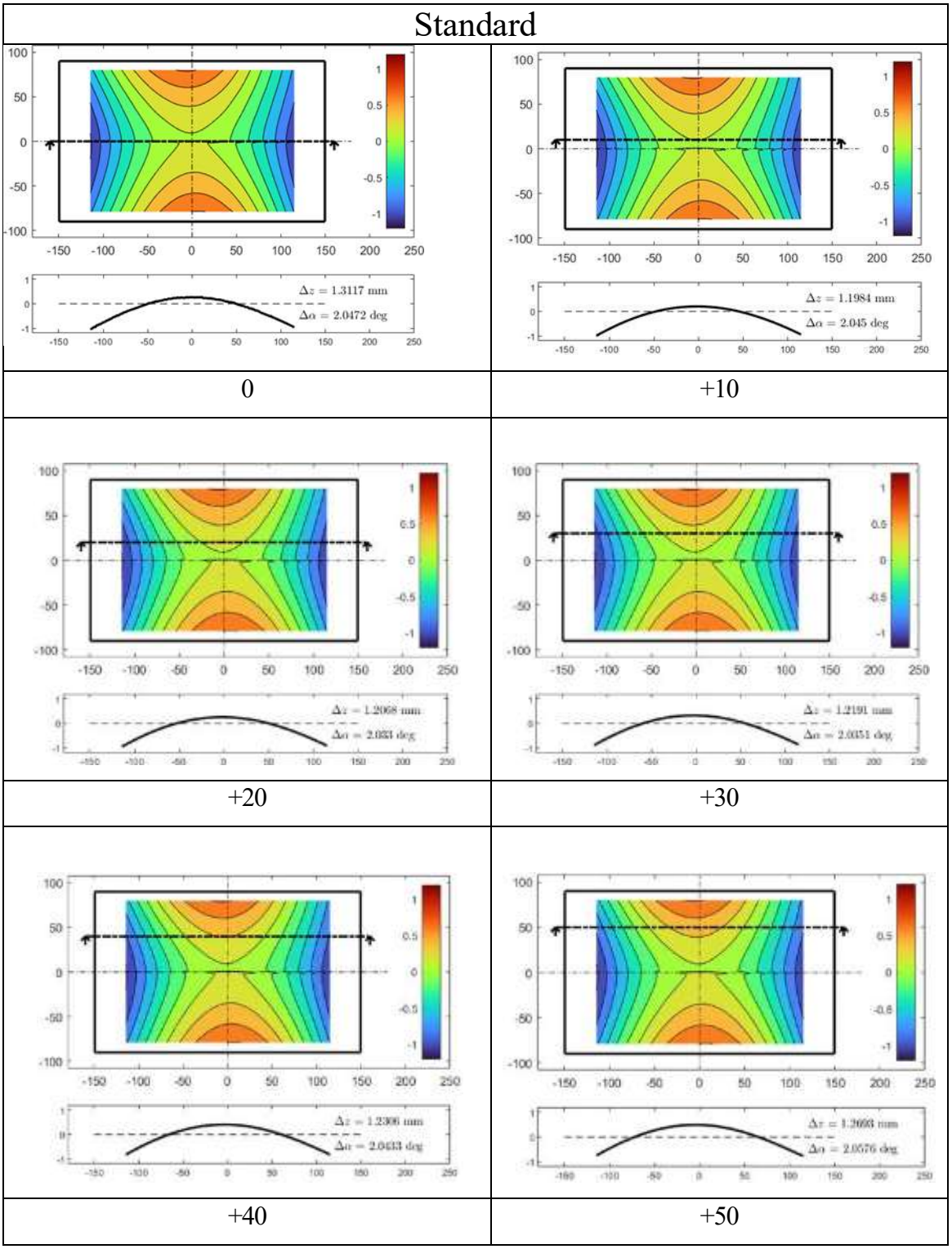

Figure 53: Distortion diagram in the positive region of the standard welded sample.

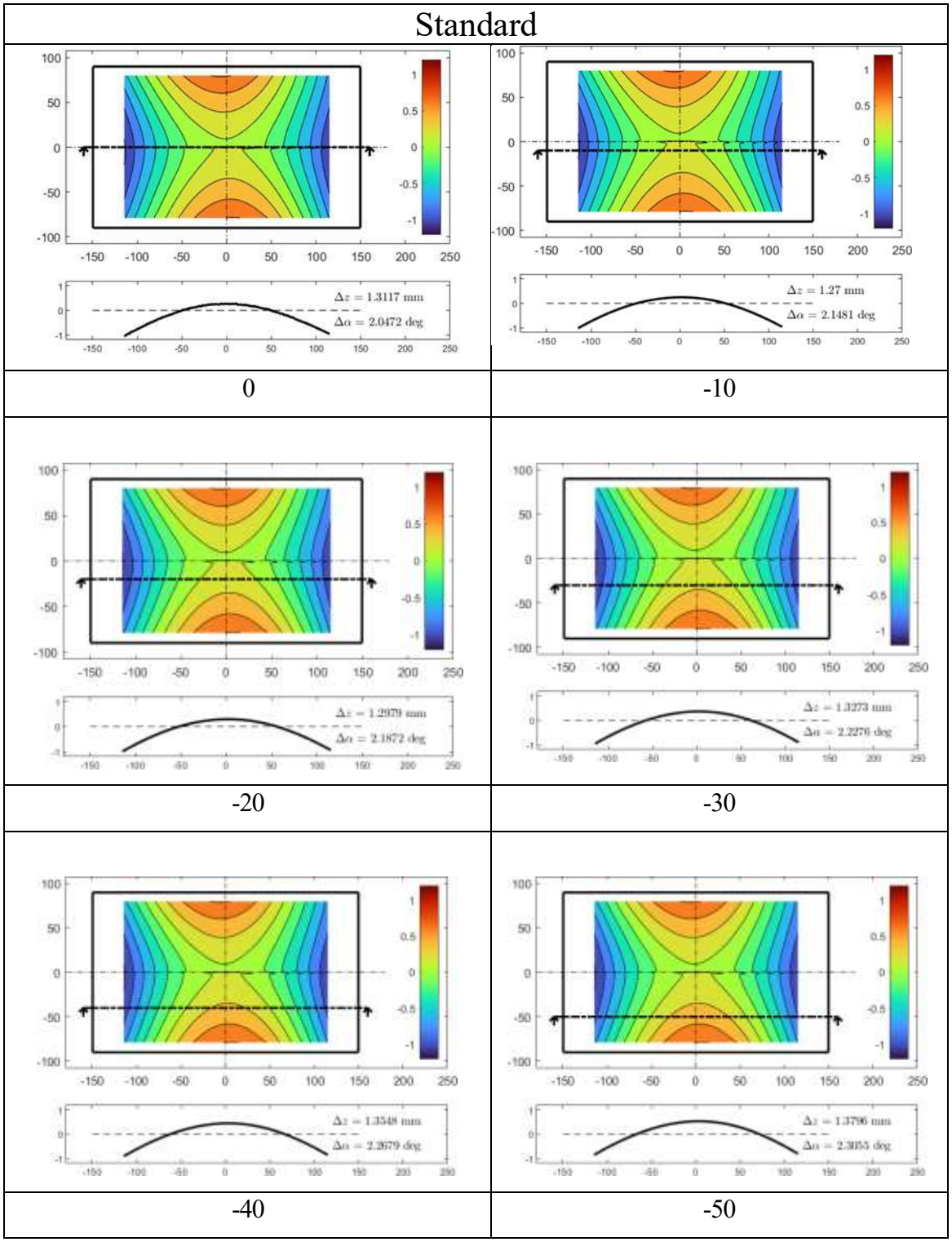

Figure 54: Distortion diagram in the negative region of the Standard welded sample.

Figure 55 illustrates the distortion angle diagram of the Standard welded sample. As seen in Figures 55 and 56 for the sample welded using the Interlocking method, changes in the angle of distortion at points 0, +10, +20, +30, +40, +50, and +60 are 1.993, 1.943, 1.957, 1.976, 2.002, and 2.027 degrees,

respectively. It is also observed that changes in the angle of distortion at points 0, -10, -20, -30, -40, -50, and -60 are 1.993, 1.996, 2.046, 2.096, 2.152, and 2.202 degrees, respectively. According to the obtained results, it is observed that as one moves away from the center, the changes in the angle of distortion increase, similar to the Interlocking welding method.

According to the obtained results, it is observed that the changes in the angle in the Standard welding state are approximately 10.5% relative to the centerline.

The changes in the height of distortion at points 0, +10, +20, +30, +40, +50, and +60 are 1.210, 1.165, 1.239, 1.318, 1.401, and 1.480 degrees, respectively. Additionally, it is observed that the changes in the height of distortion at points 0, -10, -20, -30, -40, -50, and -60 are 1.210, 1.273, 1.338, 1.406, 1.479, and 1.548 degree, respectively.

By comparing the changes in the distortion angle, it is observed that the sample welded Standard has approximately 2% more distortion compared to the sample welded Interlocking.

Longitudinal and transverse contractions during the molten and solidification cycles of the molten pool have significant effects on volume changes and the occurrence of distortions in the sheets. One of the important parameters in thermal distortion in welding is the heat input. An increase in heat input in metal welding leads to an increase in distortion in welded components. Tensile residual stress on the weld line reduces fatigue strength and ductility, especially when combined with any crack or defect related to the weld metal. To reduce some of the residual stresses resulting from the welding process, the structure undergoes deformation, leading to the creation of distortions.

There are various types of distortions, but one of the most common, especially in thin-walled structures, is buckling distortion caused by compressive stress in the base material. Buckling distortion, due to the use of new materials with high strength that allow the use of thinner sections by reducing critical buckling loads (and stresses), is increasingly common

Interlocking	
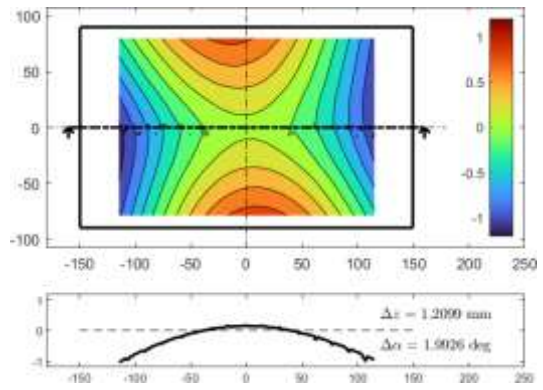	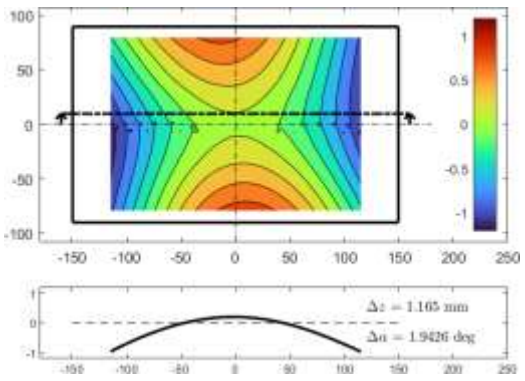
0	+10
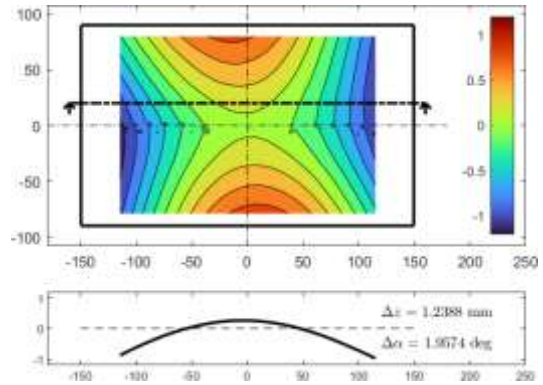	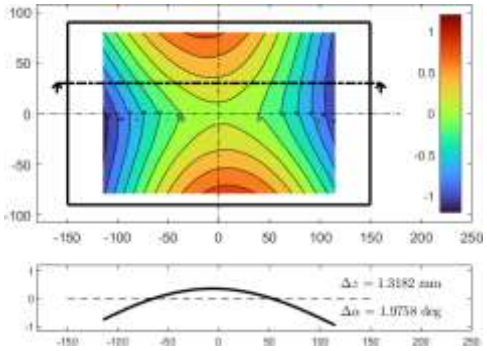
+20	+30
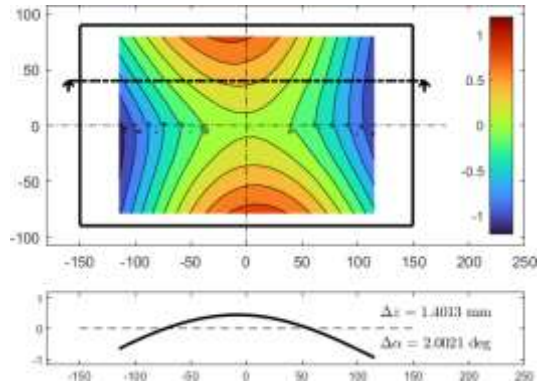	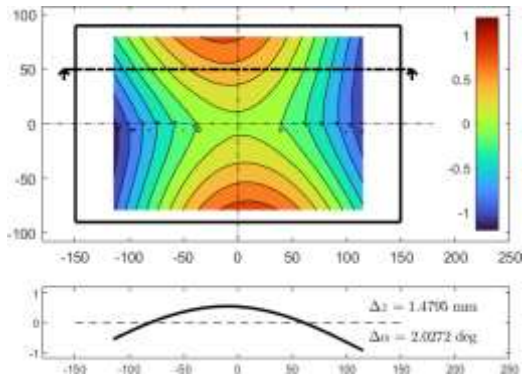
+40	+50

Figure 55: illustrates the distortion diagram in the positive region of the sample welded in an Interlocking pattern.

Interlocking	
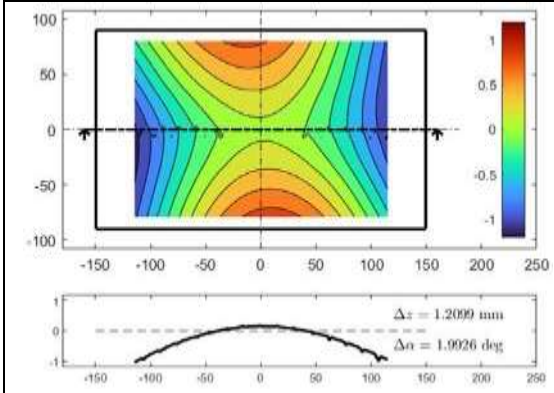	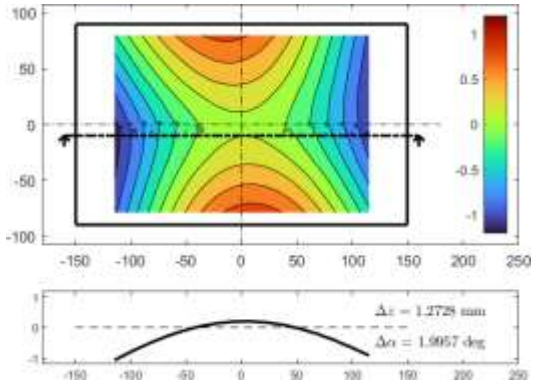
0	-10
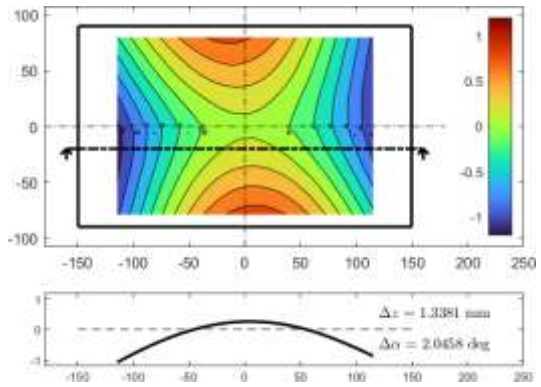	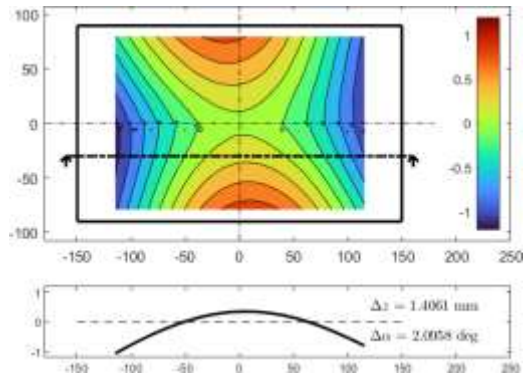
-20	-30
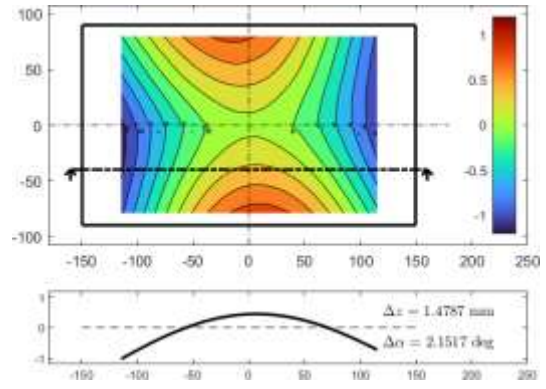	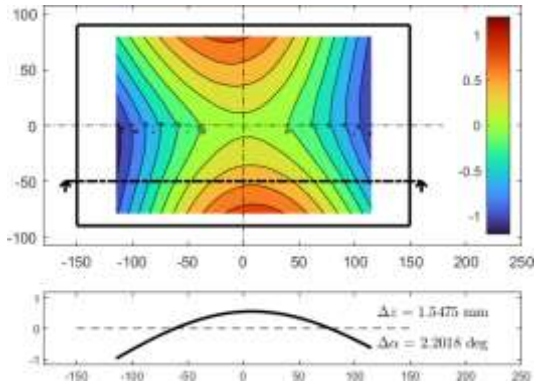
-40	-50

Figure 56: illustrates the distortion diagram in the negative region of the sample welded in an Interlocking pattern.

Chapter 5: Result Summary

5-1 Result Summary

In this research, an attempt was made to assess metallurgical and mechanical properties of the SS A304 laser butt welded joints, employing both Standard and Interlocking approaches. Additionally, the investigation involved the examination and measurement of residual stress and distortion resulting from this connection. Microstructural behavior and mechanical properties of the joint, including tensile strength, microhardness, residual stress, and distortion, were of interest.

Key findings of this research include:

1. Microstructural results indicate that the microstructure formed in the joint, using both Standard and interlocking welding methods, consists of a ferritic skeleton and a network in the austenitic phase. Microstructural results are almost identical for both welding conditions.

2. Microhardness results reveal that the microhardness of the base metal of the austenitic stainless steel is within the range of 131 Vickers, reaching approximately 221 Vickers in the center of the weld metal. This can be attributed to the formation of a skeletal ferrite phase. Moreover, the microhardness in the Interlocking welding condition is about 30 Vickers lower in the weld metal region compared to the Standard welding condition, resulting from an increase in the amount of ferrite in the weld metal of the standard welding compared to the Interlocking welding.

3. The tensile test results indicate that the yield strength of the welded specimen using the Interlocking method increased by approximately 8% compared to the specimen welded using the linear method. Additionally, the ultimate tensile strength of the specimen welded by the zigzag method increased by about 1.2% compared to the specimen welded using the Standard method.

4. Welding residual stress in the samples is tensile, and only in the heat-affected region of the Standard -welded sample, lateral residual stress is observed in a compressive manner. On average it can be argued that the longitudinal residual stresses in the welded joint with a zig-zag pattern are significantly lower than the longitudinal stresses in the welded joint with a straight pattern.

5. Results indicate that the changes in the angle in the Standard welding condition are almost equal to 12.6 % compared to the centerline, while changes in the angle in the Interlocking welding condition are approximately 10.5%.

   Considering the obtained results, it is observed that changes in height in the Standard welding condition are approximately 5.2%, while changes in the height of distortion observed in the Interlocking -welded sample are about 28.9%

6-1 Reference

[1] Javadi, Y. Akhlaghi, M. and Najafabadi, M. A. "Using finite element and ultrasonic method to evaluate welding longitudinal residual stress through the thickness in austenitic stainless steel plates" Materials Design vol. 45, pp. 628-642, 2013.

[2] Zackay, V. F. Parker, E. R. Fahr, D. and Busch, R. "The enhancement of ductility in high-strength steels", Transaction of the American society of Metals, Vol. 60, pp. 252-259, 1967.

[3] Mc Guire, M. F., Stainless steels for design engineers, Materials Park, Ohio: ASM International, 2008.

[4] Taylor and Francis Group, Steel heat treatment handbook, Portland, Oregon, U.S.A, 2007.

[5] Atlas steels technical department, "The atlas steels technical handbook of stainless steels", 2013.

[6] Michael, F. Mcguir, Stainless steels for design engineers, ASM international, 2008.

[7] William, N. Sharpe, J., handbook of Experimental Solid Mechanics, springer, 2008.

[8] David, S. A,"Ferrite morphology and variations in ferrite content in austenitic stainless steel welds", 62nd AWS Annual Meeting in Cleveland, WELDING RESEARCH SUPPLEMENT, Ohio, during April 5-10, 1981.

[9] Smith, J. J and Farrar, R. A."Influence of microstructure and composition on mechanical properties of some AI51 300 series weld metals", International Materials Reviews, Vol. 38, NO.1 25, 1993.

[10] Fuentes, G. Salas, A. Centeno, R. Del Rosario, L. "Crack growth study of dissimilar steels (Stainless - Structural) butt welded unions under cyclic loads", Journal of Procedia Engineering, Vol.10, PP. 1917–1923, 2011.

[11] Mc Guire, M. F., Stainless steels for design engineers, Materials Park, Ohio: ASM International, 2008

[12] Du, X. S. Su, Y. J. Li, J. X. Qiao, L. J. Chu, W. Y. "Stress corrosion cracking of A537 steel in simulated marine environments", Corrosion Science, Vol. 65, PP. 278–287, 2012.

[13] ASTM, A 537/A 537M, Standard Specification for Pressure Vessel Plates, Heat-Treated, Carbon-Manganese-Silicon Steel.

[14] AWS Handbook, Dissimilar metals, 7th edition, Vol. 4, 1997.

[15] Khalifeh, A. R. Dehghan, A. Hajjari, E. "Dissimilar joining of AISI 304L/St37 steels by TIG welding Process", Acta Metall. Sin. (Engl. Lett.), Vol. 26, pp. 721-727, 2013.

[16] Totten, G. Howes, M. Inoue, T., Handbook of Residual Stress and Deformation of Steel. ASM Handbook, oh Ohio, 2002.

[17] Epselis, N. Literature, "Review of Weld Stress Relieving of Transportable Pressure Vessels, ME Prac", University of Wollongong, 1996.

[18] ASM, "Metals handbook", Volume6, 9th edition, 1983.

[19] Mochizuki, M. "Control of welding residual stress for ensuring integrity against fatigue and stress–corrosion cracking", Nuclear Engineering and Designg, Vol. 237, pp. 107–123, 2007.

[20] Teng, T. L. Chang, P. H. Tseng, W. Ch. "Effect of welding sequences on residual stresses", Computers and Structures, Vol. 81, pp. 273–286, 2000.

[21] Masubuchi, K. Blodgett, O.W. Matsui, S. Ross, F.P. Tsai, C.L., "Residual stresses and distortion"., Welding handbook, 9th ed, vol. 1. Miami: American Welding Society; pp. 218–64. 1999.

[22] Ramana, P. V. Reddy, G. M. Mohandas, T. Gupta, A.V.S.S.K.S. "Microstructure and residual stress distribution of similar and dissimilar electron beam welds – Maraging steel to medium alloy medium carbon steel", Materials and Design Vol. 31, pp. 749–760, 2010.

[23] Rossini, N .S. Dassisti, M. Benyounis, K.Y. Olabi, A.G. "Methods of measuring residual stresses in components", Materials and Design, Vol. 35, pp. 572–588, 2012.

[24] H. Huanga, S. Tsutsumi, J. Wang, L. Li, H. Murakaw ," High performance computation of residual stress and distortion in laser welded 301L stainless sheets", Finite Elements in Analysis and Design, Vol. 135, pp. 1–10, 2017.

[25] A. P. Tadamalle, Y. P. Reddy, E. Ramjee and V. K. Reddy," Evaluation of Distortion and Residual Stresses in Dissimilar Metal Laser Welds"Lasers in Manufacturing and Materials Processing, 2019.

[26] Sh. Yan, Zh. Meng, B. Chen, C. Tan X. Song, Guodong Wang " Prediction of temperature field and residual stress of oscillation laser welding of 316LN stainless steel", Optics & Laser Technology, Vol. 145, pp. 107493, 2022.

[27] Z. Jiang, X. Chen, H. Li, Z. Lei, Y. Chen, S. Wu, Y. Wang, Grain refinement and laser energy distribution during laser oscillating welding of Invar alloy, Mater. Des. Vol. 186, pp. 108195, 2020.

[28] K. Hao, G. Li, M. Gao, X. Zeng, Weld formation mechanism of fiber laser oscillating welding of austenitic stainless steel, J. Mater. Process. Technol. Vol. 225, pp. 77–83, 2015.

[29] G. Xia, C. Ch., J. Jia, W. Huang, H. Liu & Y. Long," Prediction of temperature field and residual stress of oscillation laser welding of 316LN stainless steel ", Optics & Laser Technology 145(4):107493.

[30] F. Giudice and A. Sili "A theoretical approach to the residual stress assessment based on thermal field evaluation in laser beam welding", The International Journal of Advanced Manufacturing Technology, Vol. 123, pp. 2793–2808, 2022.

[31] Micro-Measurements TN-503 (2010) Measurement of residual stresses by the hole-drilling strain gauge method. Technical Note TN-503–6. Vishay Precision Group

[32] Lin YC, Chou CP (1995) Error induced by local yielding around hole in the hole drilling method for measuring residual stress of materials. Mater Sci Tech 11:600–604